

# Chapter 1

## Analysis of High Mass Drell-Yan Transverse Spin Phenomena

This chapter goes over the analysis techniques and results from the 2015 transversely polarized Drell-Yan data taking. The chapter begins by describing the data collection setup and the event selection criteria followed by the analysis techniques used to determine asymmetry amplitudes. The analysis techniques described are: the standard transverse spin-dependent asymmetry (TSA) analysis, Sec 1.2, the double ratio analysis, Sec 1.3, the  $q_T$  weighted asymmetry analysis, Sec 1.4, and finally the left-right asymmetry analysis, Sec 1.5. All of these analyses are related in that they measure TMD effects from the Drell-Yan process. For this reason the event selection and kinematical asymmetry binning described in the opening sections will be the same for all analyses in this chapter unless stated otherwise.

### 1.1 Data Sample

#### 1.1.1 Data Collection

The data sample is from the 2015 COMPASS Drell-Yan measurement. In this measurement a 190 GeV/c  $\pi^-$  beam impinged on a transversely polarized NH<sub>3</sub> target and two oppositely charged muons were detected in the spectrometer. Fig. 1.1 gives a visual of the basic setup and chapter ?? goes over the spectrometer setup and beam in more details. The COMPASS spectrometer began taking commissioning data in April of 2015. The data collected for this analysis, after the commissioning phase, is from July 8 through November 12 of 2015. The data is split into 9 periods lasting approximated 2 weeks each and labeled W07-W15. During each data period the spectrometer conditions were frozen so no detector changes could effect the spectrometer acceptance. Sec ?? describes the polarized target in more details but in short, the NH<sub>3</sub> target was split into two oppositely polarized cells separated by 20 cm with one cell polarized vertically up and one cell polarized vertically down in the lab frame. Each data period is split into two sub-periods where to reduce systematic effects of acceptance and luminosity dependencies, the polarization of both cells was flipped between sub-periods. A summary of the analysis data taking from each period is shown in Table 1.1.

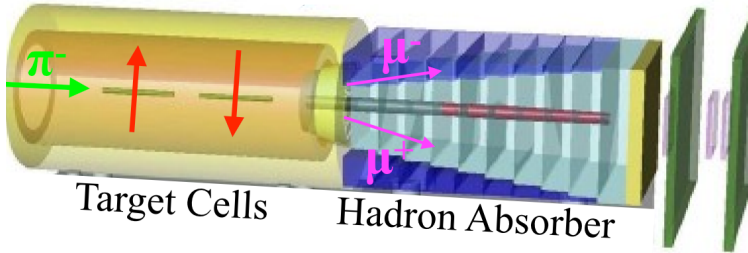


Figure 1.1: Basic pictorial setup of the 2015 COMPASS Drell-Yan data collection.

Period	Sub-period	Polarization	First-Last run	Begin date	End date
W07	one	$\downarrow\uparrow$	259363 - 259677	July 9	July 15
	two	$\uparrow\downarrow$	259744 - 260016	July 16	July 22
W08	one	$\uparrow\downarrow$	260074 - 260264	July 23	July 29
	two	$\downarrow\uparrow$	260317 - 260565	July 29	August 5
W09	one	$\downarrow\uparrow$	260627 - 260852	August 5	August 12
	two	$\uparrow\downarrow$	260895 - 261496	August 12	August 26
W10	one	$\uparrow\downarrow$	261515 - 261761	August 26	September 1
	two	$\downarrow\uparrow$	261970 - 262221	September 4	September 9
W11	one	$\downarrow\uparrow$	262370 - 262772	September 11	September 22
	two	$\uparrow\downarrow$	262831 - 263090	September 23	September 30
W12	one	$\uparrow\downarrow$	263143 - 263347	September 30	October 7
	two	$\downarrow\uparrow$	263386 - 263603	October 8	October 14
W13	one	$\downarrow\uparrow$	263655 - 263853	October 15	October 21
	two	$\uparrow\downarrow$	263926 - 264134	October 22	October 28
W14	one	$\uparrow\downarrow$	264170 - 264330	October 28	November 2
	two	$\downarrow\uparrow$	264429 - 264562	November 4	November 8
W15	one	$\downarrow\uparrow$	264619 - 264672	November 9	November 11
	two	$\uparrow\downarrow$	264736 - 264857	November 12	November 16

Table 1.1: COMPASS 2015 data taking periods

### 1.1.2 Stability Tests

To ensure the data analyzed were recorded during stable beam and spectrometer conditions, stability of the analysis data was performed on a spill-by-spill and run-by-run basis. The data was recorded in runs with a maximum of 200 spills per run. One spill can have several thousand events.

#### Bad Spill Analysis

To determine if a given spill is deemed unstable several macro variables were averaged over per spill and compared to neighboring spill averages. These macro variables were chosen specifically to be sensitive to the general stability conditions of the data collection and are listed in Table 1.1.2. The analysis criteria for an bad spill events was two oppositely charged muons. A muon is defined as having crossed 15 radiation lengths of material.

- number of beam particles divided by the number of events
- number of beam particles divided by the number of primary vertices
- number of hits per beam track divided by the number of beam particles
- number of primary vertices divided by the number of events
- number of outgoing tracks divided by the number of events
- number of outgoing particles from a primary vertex divided by the number of primary vertices
- number of outgoing particle from primary vertex divided by the number of events
- number of outgoing particles from primary vertex divided by the number of events
- number of hits from outgoing particles divided by the number outgoing particles
- number of  $\mu^+$  tracks divided by the number of events
- number of  $\mu^+$  tracks from primary vertex divided by the number of events
- number of  $\mu^-$  tracks divided by the number of events
- number of  $\mu^-$  tracks from primary vertex divided by the number of events
- $\sum \chi^2$  of outgoing particles divided by the number of outgoing particles
- $\sum \chi^2$  of all vertices divided by the number of all vertices in an event
- Trigger rates (LASxLAS, OTxLAS, LASxMT)

If the data collect was stable during a spill the average values from the macro variables in Table 1.1.2 are expected to be constant from one spill to the next. To determine if a spill was recorded in unstable conditions the spill of interest is compared with its neighboring 2500 spills occurring before and after in time. If the spill of interest is over a specified sigma deviation from any of the neighboring spills too many times, the spill is mark as a bad spill. If a spill fails this bad spill criteria for any of the macro variables in Table 1.1.2 the spill is deemed bad and not included in the analysis. The criteria for the sigma distance and number of times a spill crosses this distance to be deemed a bad are different for each data taking period. In addition to checking the nearest neighbor spills, an entire run is marked bad if the run has less than 10 spills or greater than 70% bad spills. Table 1.2 describes the bad spill impact on each period.

## Bad Run Analysis

The stability of the spectrometer is also verified by a run-by-run check in parallel to the spill-by-spill checks. The run-by-run analysis compares kinematic distributions and the average of these distributions per run to the kinematic distributions and averages from the other runs in a given period. The distributions tested are:  $x_N$ ,  $x_\pi$ ,  $x_F$ ,  $q_T$ ,  $M_{\mu\mu}$ ,  $P_{\mu^+}$ ,  $P_{\mu^-}$ ,  $P_\gamma$ ,  $P_{\pi^-}$ , and vertex x, y and z positions. The quantities in the run-by-run analysis are expected to influence the asymmetries measured, however their distributions and averages are not expected to have spin-influenced effects from the limited statistics in just a single run.

The distributions are compared with an unbinned-Kolmogorov test (UKT) and the averages over a distribution are compared based on their deviations from each other. The unbinned-Kolmogorov test is made between all the runs in a given period. A run is marked bad if it is incompatible with most of the runs in a period. Additionally, the mean for each distribution in a run is compared with the average from a given period. When an average kinematical variables from a run is more than five standard deviations from the average within a period, the run is rejected. The results of the bad spill rejection after having already applied the bad spill rejection are shown in Table 1.2.

Period	Bad Spill Rejection	Bad Spill and Bad Run Rejection
W07	11.79%	17.94%
W08	18.00%	21.19%
W09	14.76%	17.11%
W10	15.88%	17.80%
W11	22.49%	26.14%
W12	12.71%	13.79%
W13	22.32%	22.73%
W14	8.91%	10.70%
W15	3.94%	3.94%

Table 1.2: Stability analysis rejection percentages

### 1.1.3 Event Selection

The cuts in the event selection were chosen to ensure the event consisted of two oppositely charged muons resulting from a pion collision in the transversely polarized target. The event selection was initial filtered from miniDSTs to  $\mu$ DSTs where only events with at least two muons detected were kept in the  $\mu$ DSTs. The cuts used in this analysis are described in Table 1.1.3 where the event selection is performed on the  $\mu$ DSTs and the events used are from the slot1 reconstruction. A summary of the number of events remaining after the last cuts is shown in Table 1.2.

1. Two oppositely charged particles from a common best primary vertex having an invariant mass between

$4.3 \text{ GeV}/c^2$  and  $8.5 \text{ GeV}/c^2$ . A primary vertex is defined as any vertex with an associated beam particle. In case of multiple common primary vertices the best primary vertex was determined by CORAL tagging the vertex as best primary (PHAST method `PaVertex::IsBestPrimary()`). In the case that CORAL did not tag any of the common vertices as the best primary the vertex with the smallest spatial  $\chi^2$  value was used as the best primary vertex. The mass range of  $4.3 \text{ GeV}/c^2$  through  $8.5 \text{ GeV}/c^2$  is deemed the high mass range. As is shown in Fig. 1.3 this mass range corresponds over 96 % Drell-Yan events.

2. A dimuon trigger fired. A dimuon trigger firing means there are at least two particles in coincidence in this event. The dimuon triggers used were a coincidence between two particles in the large angle spectrometer, LAS-LAS trigger, or a particle in the large angle spectrometer and a particle in the Outer hodoscope, LAS-Outer trigger. The triggering process is further described in Sec ???. The LAS-Middle trigger was used as a veto on beam decay muons. A beam decay muon results from the decay of a beam pion, kaon or anti-proton into a muon depicted as  $\pi^- \rightarrow \mu^- + \bar{\nu}_{\mu^-}$ ,  $K^- \rightarrow \mu^- + \bar{\nu}_{\mu^-}$ , or  $\bar{p} \rightarrow \mu^- + \bar{\nu}_{\mu^-}$  respectively. A beam decay muon can then be in coincidence with a positive muon from another decay or strong reaction in the target resulting in an unwanted background process. The LAS-Middle trigger was used as a veto because this trigger was found to have many events resulting from a beam pion decaying to a muon.
3. Both particles are muons. A muon was defined as having crossed 30 radiation lengths of material between the particles first and last measured points. This criteria has been previously been determined to be effective at distinguishing between muons and hadrons. In the data production no detectors were used from upstream of the hadron absorber so the absorber is not included in the determination of material crossed.
4. The first measured point for both particles occurs before 300 cm and the last measured point occurs after 1500 cm. This cut ensures both particles have positions upstream of the first spectrometer magnet and downstream of the first muon filter.
5. The timing of both muons is defined. This checks that the time relative to the trigger time is determined for both muons so further timing cuts can be performed.
6. Both muons are in time within 5 nanoseconds. This track time for each muon is defined relative to the trigger time as in the previous cut. This cut rejects uncorrelated muons.
7. The muon track's spacial reduced  $\chi^2$  are individually less than 10. This cut ensures track quality.

8. A validation that each muon crossed the trigger it was associated as having triggered. This trigger validation cut was performed by extrapolating (PHAST Method PaTrack::Extrapolate()) each muon track back to the two hodoscopes it fired and determining if the muon crossed the geometric acceptance of both of these hodoscopes.
9. The event does not occur in the bad spill or run list. Many tests were performed to test the basic stability of the spectrometer and beam as described in Sec 1.1.2. The spills placed on the bad spill list were deemed to occur during unstable data taking conditions.
10. The Drell-Yan kinematics are physical. That is  $0 < x_\pi x_N < 1$  and  $-1 < x_F < 1$ .
11. The transverse momentum of the virtual photon,  $q_T$ , is between 0.4 and 5.0 GeV/c. The lower limit ensures the azimuthal angular resolution is sufficient and the upper cut further ensures the kinematic distributions are physically possible and not badly reconstructed events.
12. The vertex originated within the z-positions of the transversely polarized target cells defined by the target group.  $-294.5 \text{ cm} < Z_{\text{vertex}} < -239.3 \text{ cm}$  for the upstream target and  $-219.5 \text{ cm} < Z_{\text{vertex}} < -164.3 \text{ cm}$  for the downstream target.
13. The vertex is within the radius of the polarized target measured to be 1.9 cm.

Cuts	W07	W08	W09	W10	W11	W12	W13	W14	W15	WAll	Remaining
High Mass $\mu^- \mu^+$ with a common best primary vertex	19410	19184	19654	20707	31371	23563	20561	13154	7697	175301	100.00 %
Good Spills	15947	14899	16217	16895	23041	20184	16026	11796	7422	142427	81.70 %
$0 < x_\pi x_N < 1, -1 < x_F < 1$	15932	14886	16200	16885	23022	20171	16013	11794	7414	142317	81.70 %
$0.4 < q_T < 5(\text{GeV}/c)$	14342	13385	14609	15239	20667	18101	14365	10588	6636	127932	60.75 %
Z Vertex within NH <sub>3</sub>	4256	4024	4330	4552	6369	5503	4411	3130	2028	38603	15.05 %
Vertex Radius < 1.9cm	4175	3950	4257	4474	6252	5414	4334	3078	1987	37921	12.21 %

Figure 1.2: Numbers of selected di-muon events in this analysis of 2015 COMPASS data

#### 1.1.4 Binning

The asymmetries are measured in bins of  $x_N$ ,  $x_\pi$ ,  $x_F$ ,  $q_T$ , and  $M_{\mu\mu}$ .  $x_N$  and  $x_\pi$  are the momentum fractions of the target nucleon and beam pion respectively,  $x_F = x_\pi - x_N$ ,  $q_T$  is the transverse momentum of the virtual photon and  $M_{\mu\mu}$  is the invariant mass of the di-muon. The binning was determined by requiring equal statistical population in each kinematic bin. In addition, the asymmetries are determined in an integrated bin using all the analysis data. The analyzes binning limits are summarized in Table 1.3.

Kinematics	Lowest limit	Upper limit bin 1	Upper limit bin 2	Upper limit bin 3
$x_N$	0.0	0.13	0.19	1.0
$x_\pi$	0.0	0.40	0.56	1.0
$x_F$	-1.0	0.22	0.41	1.0
$q_T$ (GeV/c)	0.4	0.86	1.36	5.0
$M_{\mu\mu}$ (GeV/c <sup>2</sup> )	4.3	4.73	5.50	8.5

Table 1.3: Analysis binning limits

### 1.1.5 Analysis Notation

Table 1.4 summarizes the general notations used in the asymmetry analysis definitions and derivations used throughout this chapter.

Table 1.4: Notations used for defining the asymmetry analysis

Notation	Description
1(2)	target cell number. 1=upstream, 2=downstream
$\uparrow (\downarrow)$	target cell vertical polarization direction, up(down)
$ S_T $	fraction of polarized target nucleons
$l(r)$	virtual photon detected left(right) of spin
$J(S)$	spectrometer Jura(Saleve) side meaning west(east) side

## 1.2 Transverse Spin-Dependent Asymmetries

This section describes the standard TSA analysis for which the results are published in reference [1]. The main motivation for this analysis was to conclude on the sign flip of the Sivers function flip between the Drell-Yan and SIDIS processes using data from the same experimental setup for both processes. The results shown are those determined by the COMPASS Drell-Yan analysis subgroup.

The kinematical distributions shown for this analysis are the same as for the remaining analyses in this chapter. This results from the fact that all the analyses in this chapter use the same event selection and cuts. The only exception to this is for the  $q_T$ -weighted analysis, Sec 1.4, which cannot cut on  $q_T$  and therefore has a different  $q_T$  distribution as is explained in Sec 1.4.1.

As was noted in the event selection 1.1.3, the data considered are in the invariant mass range [4.3-8.5 GeV/c<sup>2</sup>]. Fig. 1.3 shows the invariant mass range from the 2015 COMPASS data. All cuts except a cut on invariant mass are included in Fig. 1.3 and as well a fit to show the background processes is included.

The fit is determined from Monte-Carlo data and combinatorial background analysis. The Monte-Carlo data simulated all hard processes which decay to two oppositely charged muons and can be reconstructed in the COMPASS spectrometer. Combinatorial background analysis estimates the background as  $N_{combinatorial} =$

$2\sqrt{N_{\mu^+\mu^+}N_{\mu^-\mu^-}}$ . As can be seen in Fig. 1.3, there are two distinguishable background peaks. The lower mass peak at about  $3 \text{ GeV}/c^2$  corresponds to  $\text{J}/\Psi$  production and the higher mass peak at around  $3.6 \text{ GeV}/c^2$  corresponds to  $\Psi'$  production. All the analyses in this chapter use the mass range between  $4.3$  and  $8.5 \text{ GeV}/c^2$  and as Fig. 1.3 shows, the Drell-Yan process dominates in this mass range. The background percentage was estimated to be below  $4\%$  in this mass range.

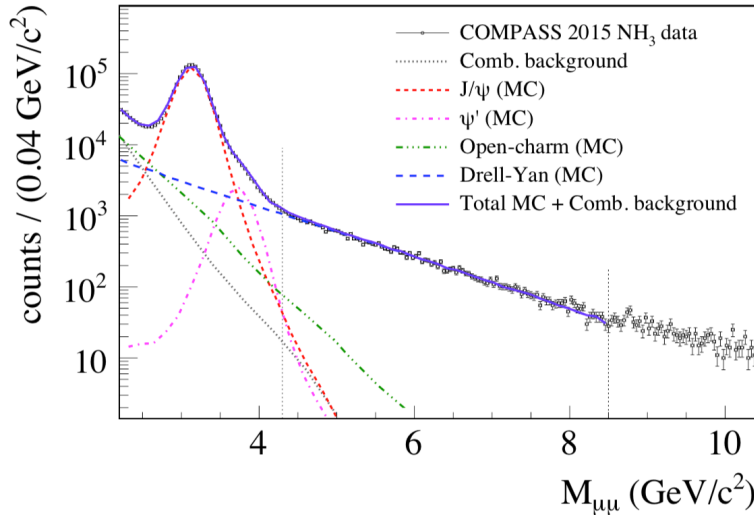
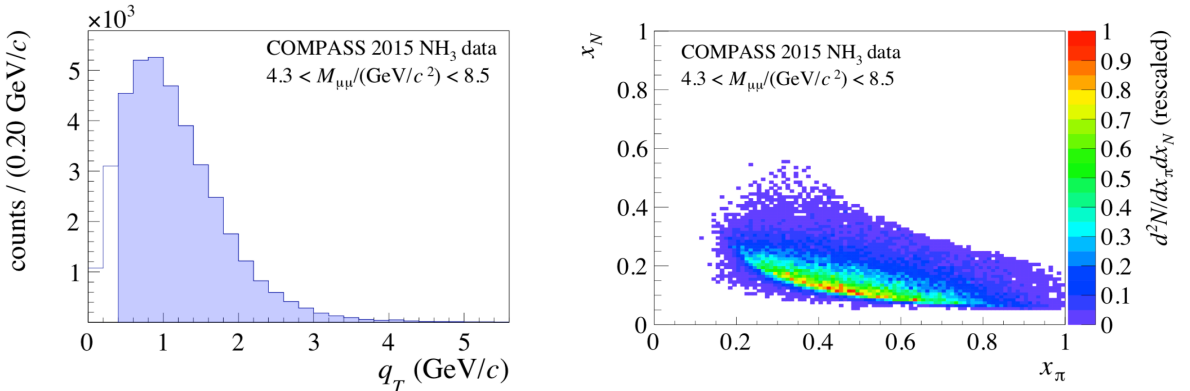


Figure 1.3: The 2015 COMPASS invariant dimuon mass distribution and a fit to this data. The data fit is from Monte-Carlo and combinatorial background analysis and is provided to show the background processes. This image is taken from [1].

Fig. 1.4a shows the transverse virtual photon momentum,  $q_T$ , distribution. With the cut on  $q_T$  between  $[0.4\text{-}5(\text{GeV}/c)]$ , the average  $q_T$  is  $1.2 \text{ GeV}/c$  while on the other hand the average  $M_{\mu\mu}$  is  $5.3 \text{ GeV}/c^2$ . As stated in chapter ??, the regime where TMD functions are the theoretical model for parton distributions is when  $q_T \ll M_{\mu\mu}$ . While the average  $q_T$  is less than the average  $M_{\mu\mu}$ , it is not excluded that the results in this chapter are outside of the TMD regime. Nevertheless all the results presented in this chapter are determined assuming the TMD description is valid.

The distribution of  $x_\pi$  versus  $x_N$  is shown in Fig. 1.4b. The Bjorken-x of the proton,  $x_N$ , is almost exclusively above  $0.1$  and as well Bjorken-x for the pion,  $x_\pi$  is in its valence region. For these reasons it is safe to say that the Drell-Yan reaction studied in the following analyses is the result of the pion's anti-u-quark annihilating with the proton's u-quark.

The results from TSA analysis are determined from an extended unbinned maximum likelihood fit to the data. The dilution and depolarization values are determined on an event by event basis unlike the other analyses in this chapter. The released integrated results for the leading order and sub-leading order TSAs are shown in Fig. 1.5. The leading order TSAs are non-zero with approximate significances of: 1 sigma for



(a) The  $q_T$  distribution where the shaded region shows the data used in the high mass analysis and the unshaded region shows the full distribution without a  $q_T$  cut. This image is taken from [1].

(b) The 2-dimensional distribution of  $x_\pi$  vs.  $x_N$ . Both  $x_\pi$  and  $x_N$  are safely in their respective valence regions. This image is taken from [1].

the Sivers TSA,  $A_T^{\sin(\phi_S)}$ , 1.2 sigma for the Pretzelosity TSA,  $A_T^{\sin(2\phi_{CS}+\phi_S)}$  and 2 sigma for the transversity TSA,  $A_T^{\sin(2\phi_{CS}-\phi_S)}$ .

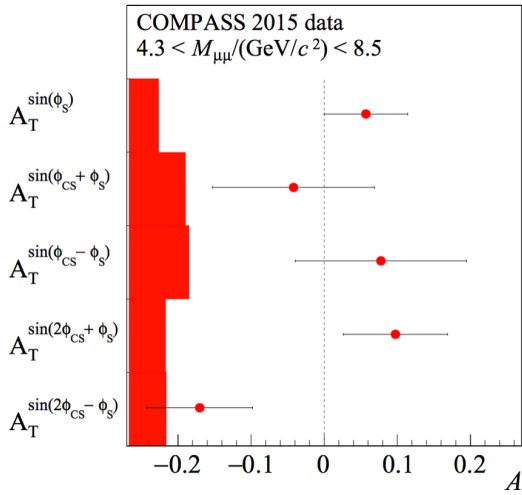


Figure 1.5: The integrated TSAs with statistical and systematic error bars.  $A_T^{\sin(\phi_S)}$ ,  $A_T^{\sin(2\phi_{CS}+\phi_S)}$ , and  $A_T^{\sin(2\phi_{CS}-\phi_S)}$  are leading order TSAs and  $A_T^{\sin(\phi_{CS}+\phi_S)}$  and  $A_T^{\sin(\phi_{CS}-\phi_S)}$  are sub-leading order TSAs.

The comparison of the Sivers TSA,  $A_T^{\sin(\phi_S)}$ , with the expected sign flip is shown in Fig. 1.6. The positive solid theory curves show the expected Sivers TSA assuming the Sivers function flips sign between Drell-Yan and SIDIS. The main difference in these three theory curves is the  $Q^2$  evolution which is also the main uncertainty in each prediction. As can be seen the Sivers TSA is compatible with the expected sign change. However, the error bars on the Sivers asymmetry amplitude are too large to conclusively distinguish between the three theory curves or even to conclusively conclude on the sign change between Drell-Yan and SIDIS.

That being said, the amplitude  $A_T^{\sin(\phi_S)}$  is 2 sigma away from being incompatible with a sign flip.

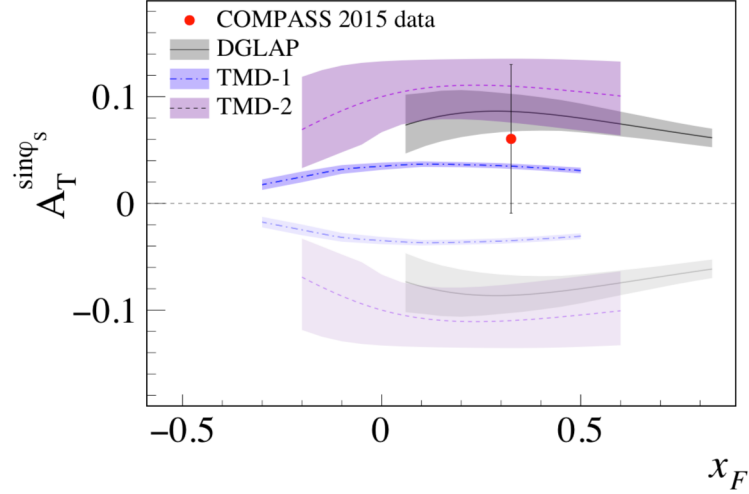


Figure 1.6: The Sivers TSA along with theory curves for the expected sign change (solid curves) and without the sign change (opaque curves). Theory curves and uncertainties are calculated using  $Q^2$  evolution from DGLAP [2], TMD-1 [3], TMD-2 [4]. This image is taken from [1].

### 1.3 Double Ratio Analysis

The double ratio method is used to determine spin-dependent asymmetry amplitudes. This means the asymmetry amplitudes  $A_T^{\sin\phi_S}$ ,  $A_T^{\sin(2\phi+\phi_S)}$  and  $A_T^{\sin(2\phi-\phi_S)}$  can be determined from the 2015 transversely polarized Drell-Yan data. The benefit of this method is that the spectrometer acceptance does not effect the determination of the asymmetry amplitudes. The author of this thesis performed the analysis in this section and found results consistent with those determined from TSA analysis.

#### 1.3.1 Asymmetry Extraction

The double ratio is defined as

$$R_D(\Phi) = \frac{N_1^\uparrow(\Phi)N_2^\uparrow(\Phi)}{N_1^\downarrow(\Phi)N_2^\downarrow(\Phi)}, \quad (1.1)$$

where  $N$  represents the counts, 1(2) is the upstream(downstream) target cell and  $\uparrow(\downarrow)$  denotes the transverse polarization direction. The number of counts,  $N(\Phi)$ , is defined as

$$N(\Phi) = L * \sigma(\Phi) * a(\Phi), \quad (1.2)$$

where  $L$  is the luminosity,  $\sigma$  is the cross-section and  $a$  is the spectrometer acceptance. In Eq. 1.2 the acceptance is a function of detector efficiencies and the spectrometer acceptance. When assuming the spin-dependent Drell-Yan cross-section, Eq. ??, the number of counts,  $N(\Phi)$ , can be written

$$N(\Phi) = a(\Phi)L\sigma_U \left( 1 \pm D_{[\theta]} |S_T| A_T^w \sin(\Phi) \right). \quad (1.3)$$

where  $+(-)$  is for target polarized up(down),  $D_{[\theta]}$  is the depolarization factor and  $|S_T|$  is the target polarization percentage. The depolarization factor,  $D_{[\theta]}$  is defined in Eq. ???. It can be thought of as the probability for the virtual photon to decay and produce such an asymmetry amplitude to that for a transversely polarized photon decay. The target polarization percentage,  $|S_T|$  is defined as  $fP$ , where  $f$  is the dilution factor, Eq. ??, and  $P$  is the target polarization percentage. Therefore the double ratio can be written

$$\begin{aligned} R_D(\Phi) &= \frac{a_1^\uparrow(\Phi)L_1^\uparrow\sigma_U \left( 1 + D_{[\theta]1}^\uparrow |S_{T1}^\uparrow| A_T^w \sin(\Phi) \right) a_2^\uparrow(\Phi)L_2^\uparrow\sigma_U \left( 1 + D_{[\theta]2}^\uparrow |S_{T2}^\uparrow| A_T^w \sin(\Phi) \right)}{a_1^\downarrow(\Phi)L_1^\downarrow\sigma_U \left( 1 - D_{[\theta]1}^\downarrow |S_{T1}^\downarrow| A_T^w \sin(\Phi) \right) a_2^\downarrow(\Phi)L_2^\downarrow\sigma_U \left( 1 - D_{[\theta]2}^\downarrow |S_{T2}^\downarrow| A_T^w \sin(\Phi) \right)} \\ &= \left( \frac{a_1^\uparrow(\Phi)a_2^\uparrow(\Phi)}{a_1^\downarrow(\Phi)a_2^\downarrow(\Phi)} \right) \left( \frac{L_1^\uparrow L_2^\uparrow}{L_1^\downarrow L_2^\downarrow} \right) \frac{\left( 1 + D_{[\theta]1}^\uparrow |S_{T1}^\uparrow| A_T^w \sin(\Phi) \right) \left( 1 + D_{[\theta]2}^\uparrow |S_{T2}^\uparrow| A_T^w \sin(\Phi) \right)}{\left( 1 - D_{[\theta]1}^\downarrow |S_{T1}^\downarrow| A_T^w \sin(\Phi) \right) \left( 1 - D_{[\theta]2}^\downarrow |S_{T2}^\downarrow| A_T^w \sin(\Phi) \right)}. \end{aligned} \quad (1.4)$$

As is described in Sec 1.1.1, the data is collected in two week periods where the conditions of the spectrometer are frozen for each data taking period. For this reason the following reasonable acceptance assumption is made

$$\frac{a_1^\uparrow(\Phi)a_2^\uparrow(\Phi)}{a_1^\downarrow(\Phi)a_2^\downarrow(\Phi)} = C. \quad (1.5)$$

where  $C$  is a constant. In addition  $L_2^{\downarrow(\uparrow)} = rL_1^{\uparrow(\downarrow)}$  where  $r$  is a constant reduction factor and therefore the luminosity terms cancel out as

$$\frac{L_1^\uparrow L_2^\uparrow}{L_1^\downarrow L_2^\downarrow} = \frac{L_1^\uparrow r L_1^\downarrow}{L_1^\downarrow r L_1^\uparrow} = 1. \quad (1.6)$$

Finally the asymmetry amplitudes and target polarizations are assumed to be small so the double ratio can be simplified to

$$\begin{aligned}
R_D(\Phi) &= C \frac{\left(1 + D_{[\theta]1}^{\uparrow} |S_{T1}^{\uparrow}| A_T^w \sin(\Phi)\right) \left(1 + D_{[\theta]2}^{\uparrow} |S_{T2}^{\uparrow}| A_T^w \sin(\Phi)\right)}{\left(1 - D_{[\theta]1}^{\downarrow} |S_{T1}^{\downarrow}| A_T^w \sin(\Phi)\right) \left(1 - D_{[\theta]2}^{\downarrow} |S_{T2}^{\downarrow}| A_T^w \sin(\Phi)\right)} \\
&\approx C \frac{1 + \left[D_{[\theta]1}^{\uparrow} |S_{T1}^{\uparrow}| + D_{[\theta]2}^{\uparrow} |S_{T2}^{\uparrow}|\right] A_T^w \sin(\Phi)}{1 - \left[D_{[\theta]1}^{\downarrow} |S_{T1}^{\downarrow}| + D_{[\theta]2}^{\downarrow} |S_{T2}^{\downarrow}|\right] A_T^w \sin(\Phi)} \\
&\approx C \left(1 + \left[D_{[\theta]1}^{\uparrow} |S_{T1}^{\uparrow}| + D_{[\theta]2}^{\uparrow} |S_{T2}^{\uparrow}|\right] A_T^w \sin(\Phi)\right) \left(1 + \left[D_{[\theta]1}^{\downarrow} |S_{T1}^{\downarrow}| + D_{[\theta]2}^{\downarrow} |S_{T2}^{\downarrow}|\right] A_T^w \sin(\Phi)\right) \\
&\approx C \left(1 + \left[D_{[\theta]1}^{\uparrow} |S_{T1}^{\uparrow}| + D_{[\theta]2}^{\uparrow} |S_{T2}^{\uparrow}| + D_{[\theta]1}^{\downarrow} |S_{T1}^{\downarrow}| + D_{[\theta]2}^{\downarrow} |S_{T2}^{\downarrow}|\right] A_T^w \sin(\Phi)\right).
\end{aligned} \tag{1.7}$$

Then making the assumption that the polarizations,  $S_T$ , and depolarization factors,  $D_\Phi$  are approximately constant throughout a data period, the asymmetry amplitude of interest can be determined by fitting the double ratio with the function

$$f(\Phi) = [p0](1 + 4[p1]\sin(\Phi)), \tag{1.8}$$

where  $[p0]$  and  $[p1]$  are fit parameters and  $[p1]$  represents the asymmetry amplitude of interest. The  $[p1]$  parameter is later corrected for average polarization and depolarization factors.

The double ratio,  $R_D$ , is determined as a function of  $\Phi$  where the angle  $\Phi$  depends on which asymmetry amplitude is being determined. The assumption made in the measured counts formula, Eq. 1.3, is that all angles except the spin-dependent  $\Phi$  angle are integrated over. When this is the true, all the Drell-Yan cross-section fourier components integrate to zero except the constant term. The following table, Table 1.5, lists which  $\Phi$  angle is used to determine which spin-dependent asymmetry amplitude.

Table 1.5: Measured counts as a function of each  $\Phi$  angle

Asymmetry Amplitude	Corresponding TMD Function	$\Phi$ Angle	$\Phi$ Range (radians)
$A_T^{\sin(\phi_S)}$	Sivers	$\phi_S$	$[-\pi, \pi]$
$A_T^{\sin(2\phi - \phi_S)}$	Transversity	$2\phi - \phi_S$	$[-3\pi, 3\pi]$
$A_T^{\sin(2\phi + \phi_S)}$	Preztelosity	$2\phi + \phi_S$	$[-3\pi, 3\pi]$

The variance of the double ratio, assuming Poisson counting statistics, is

$$\sigma_{R_D}^2 = R_D^2(\Phi) \left( \frac{1}{N_1^{\uparrow}(\Phi)} + \frac{1}{N_2^{\uparrow}(\Phi)} + \frac{1}{N_1^{\downarrow}(\Phi)} + \frac{1}{N_2^{\downarrow}(\Phi)} \right). \tag{1.9}$$

### 1.3.2 Results

The results of the asymmetry amplitudes are determined in each of the nine periods and then combined as a weighted average. The asymmetries are calculated this way to minimize the effects of acceptance changes

between periods as the spectrometer was kept stable within each period but had the options for detector changes and repairs between periods. As well this weighted average method allows for future measurements to be combined as a weighted average with the final overall results without the need to know individual period results. This resulting asymmetry amplitudes are determined from a weighted average as

$$A = \frac{\sum_{\text{period}} A_{\text{period}} \sigma_{\text{period}}^{-2}}{\sum_{\text{period}} \sigma_{\text{period}}^{-2}}, \quad \delta A = \sqrt{\sum_{\text{period}} \frac{1}{\sigma_{\text{period}}^{-2}}}. \quad (1.10)$$

For each period and each kinematical bin, the asymmetry is determined by fitting the double ratio and with Eq. 1.8. The results of the fit actually determines the quantity

$$A_T^w \langle D_{[\theta]} \rangle \langle |S_T| \rangle. \quad (1.11)$$

The asymmetry amplitude is ultimately determined by dividing the fit results by the average polarization and depolarization values per period.

To determine the asymmetry amplitude, the double ratio is binned in eight bins in  $\Phi$ . Eight bins are chosen due to the low statistics from Drell-Yan data. Fig. 1.7 shows an example of the binned double ratio and fit results.

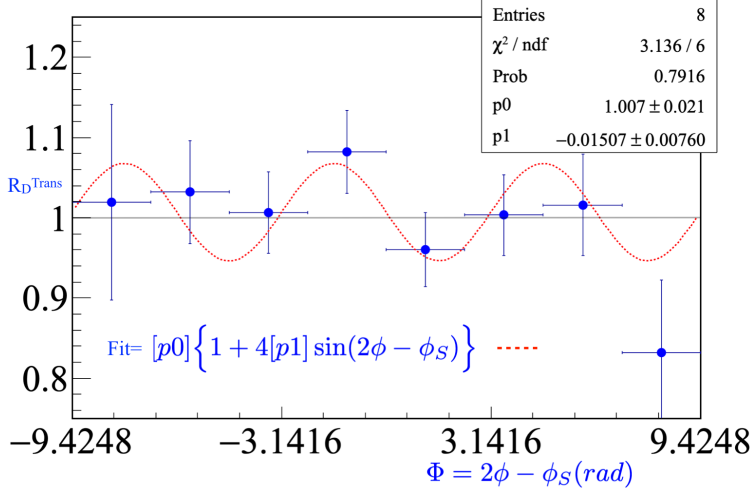


Figure 1.7: An example double ratio and corresponding fit (red) to determine the amplitude  $A_T^{\sin(2\phi-\phi_S)}$

The results for all the spin-dependent asymmetry amplitudes are shown in Fig. 1.8. As can be seen, the significance of the integrated asymmetry amplitudes is: over 1 sigma above zero for the Sivers,  $A_T^{\sin \phi_S}$ , over 3 sigma above zero for Preztelosity,  $A_T^{\sin(2\phi+\phi_S)}$ , and 3 sigma below zero for transversity,  $A_T^{\sin(2\phi-\phi_S)}$ .

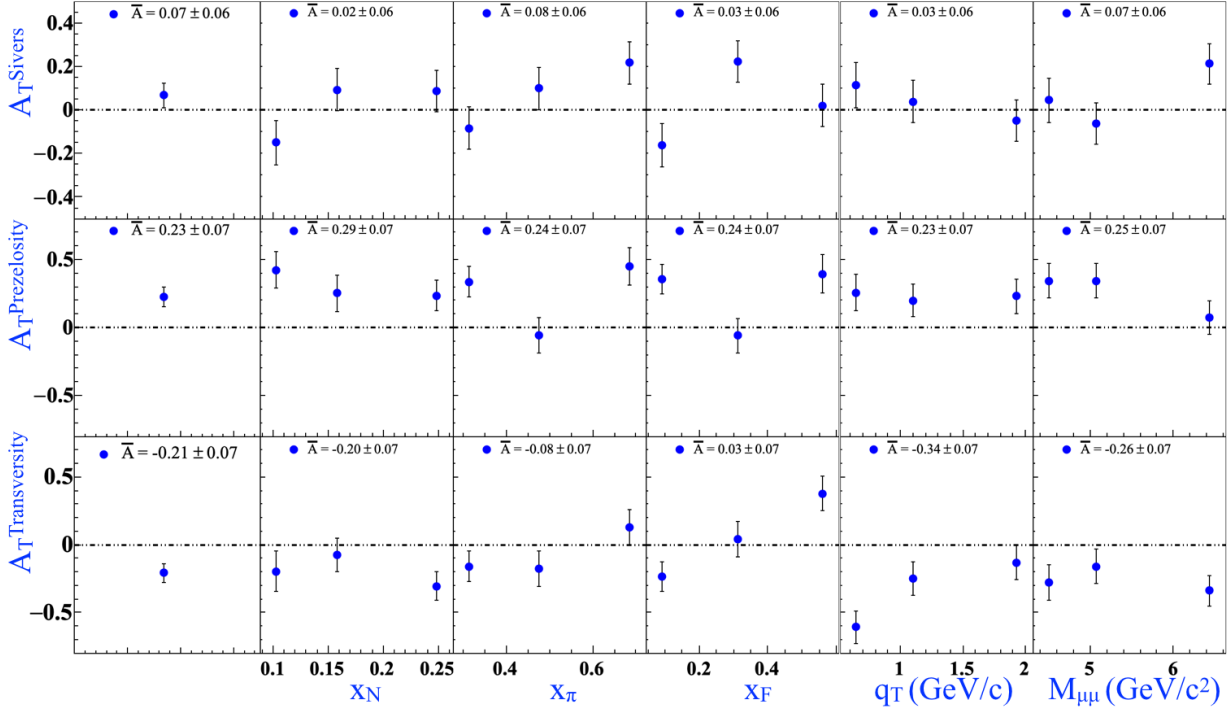


Figure 1.8: The results and statistical error bars for the transverse spin-dependent asymmetry amplitudes  $A_T^{\sin \phi_S}$  (top),  $A_T^{\sin(2\phi+\phi_S)}$  (middle) and  $A_T^{\sin(2\phi-\phi_S)}$  (bottom) determined from the double ratio method.

## 1.4 $q_T$ -Weighted Asymmetries

The  $q_T$  weighting asymmetries analysis is used to determine three asymmetry amplitudes related to TMD functions. This analysis determined the three amplitudes:  $A_T^{\sin(\phi_S)q_T/M_N}$ ,  $A_T^{\sin(2\phi+\phi_S)q_T^3/(2M_\pi M_N^2)}$  and  $A_T^{\sin(2\phi-\phi_S)q_T/M_\pi}$  which are related to the Sivers, Prezelosity and transversity TMD PDFs respectively.

The theoretical introduction and motivation for measuring  $q_T$ -weighted asymmetries is provided in Sec ???. The author of this thesis was a cross checker for the  $q_T$ -weighted asymmetry results which is a required step for any results to become public. For the full details of the  $q_T$ -weighted analysis see reference [5].

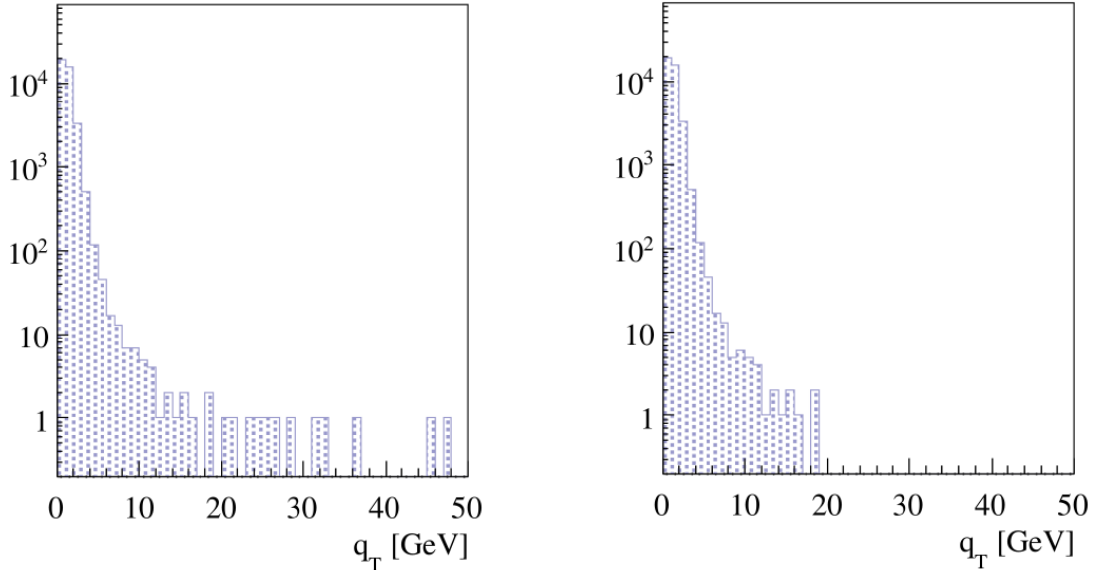
### 1.4.1 Event Selection

The results for this analysis were released prior to the slot1 reconstruction production and therefore this analysis uses the t3 reconstruction. For  $q_T$ -weighted asymmetries the results depend on the full range of the  $q_T$  distribution. In the other analyses in this chapter however, a cut was placed on high and low  $q_T$  values to ensure better azimuthal angular resolution and quality reconstructed events. This cut cannot be applied for  $q_T$ -weighted analysis because it will effect the weighting used to determine the asymmetry. On the other hand the combinatorial background and badly reconstructed events from the high  $q_T$  phase space should be

cut. The next section goes into the details and the remedy for a  $q_T$  related cut. All of the other cuts from Sec 1.1.3 are the same except for this  $q_T$  cut. Table 1.10 provides the final cut order and the remaining statistics after each cut for this  $q_T$ -weighted analysis.

### High $q_T$

The  $q_T$  distribution without any  $q_T$  cuts is shown in Fig. 1.9a. As can be seen the  $q_T$  distribution reaches values much higher than the maximum 5 GeV/c cut from the other analyses in this chapter. The most fundamental problem with this  $q_T$  distribution is that some of the events violate conservation of momentum. A first remedy to the high  $q_T$  values then is to add a cut which demands momentum conservation. This is achieved by demanding that the momentum sum of the detected muons is physically possible,  $\ell^+ + \ell^- < 190$  GeV/c. Note that this cut does not take into account the momentum spread of the beam due to the fact that the beam momentum spread is expected to be small. Fig. 1.9b shows how this cut effects the  $q_T$  distribution. As can be seen,  $q_T$  still reaches values much higher than the 5 GeV/c cut from the other TMD analyses. The remaining high  $q_T$  events still have the potential to be poorly reconstructed events or combinatorial background and for this reason an additional cut was put on the individual muons transverse momentum such that  $\ell_T^\pm < 7$  GeV/c.



(a)  $q_T$  distribution without cuts on  $q_T$ . All other cuts expect the  $q_T$  cut from table 1.1.3 are applied. This image is from [5]

(b)  $q_T$  distribution after the momentum conservation cut is added,  $\ell^+ + \ell^- < 190$  GeV/c. All other cuts expect the  $q_T$  cut from table 1.1.3 are applied. This image is from [5]

Cuts	Events	% Remaining
$\mu^+ \mu^-$ from best primary vertex, $4.3 < M_{\mu\mu} < 8.5 \text{ GeV}/c^2$	1,159,349	100.00
Triggers: (2LAS or LASxOT) and not LASxMiddle	868,291	74.89
$Z_{first} < 300 \text{ cm}, Z_{last} > 1500 \text{ cm}$	784,379	67.66
$\Delta t$ defined	776,643	66.99
$ \Delta t  < 5 \text{ ns}$	337,081	32.18
$\chi^2_{track}/\text{ndf} < 10$	370,054	31.92
$\ell^+ + \ell^- < 190 \text{ GeV}/c$	219,304	18.92
$\ell_T^\pm < 7 \text{ GeV}/c$	219,014	18.89
Trigger Validation	168,939	14.57
Good Spills	137,812	11.89
$0 < x_\pi x_N < 1, -1 < x_F < 1$	137,802	11.89
Z Vertex within NH <sub>3</sub>	42,646	3.68
Vertex Radius < 1.9cm	39,088	3.37

Figure 1.10: Event selection statistics for  $q_T$ -weighed asymmetry analysis from all periods combined

### 1.4.2 Binning

As with the other analyses in this chapter, the asymmetry is determined in bins of the Drell-Yan physical kinematic variables:  $x_N$ ,  $x_\pi$ ,  $x_F$  and  $M_{\mu\mu}$  and an overall integrated value. No  $q_T$  binning is used however, because a full integrating of the  $q_T$  variable needs to be taken into account to form the weighted asymmetry.

### 1.4.3 Asymmetry Method

The weighted asymmetry amplitudes  $A_T^{\sin(\phi_S)q_T/M_N}$ ,  $A_T^{\sin(2\phi+\phi_S)q_T^3/(2M_\pi M_N^2)}$  and  $A_T^{\sin(2\phi-\phi_S)q_T/M_\pi}$  are all determined using a modified double ratio. As with the double ratio method from Sec 1.3, the modified double ratio does not depend on the spectrometer acceptance. The modified double ratio is defined as

$$R_{DM}^W(\Phi) = \frac{N_1^{\uparrow W} N_2^{\uparrow W} - N_1^{\downarrow W} N_2^{\downarrow W}}{\sqrt{(N_1^{\uparrow W} N_2^{\uparrow W} + N_1^{\downarrow W} N_2^{\downarrow W})(N_1^{\uparrow} N_2^{\uparrow} + N_1^{\downarrow} N_2^{\downarrow})}}, \quad (1.12)$$

where similar notation is used from the previous analyses where  $\uparrow(\downarrow)$  is the transverse polarization direction, 1(2) denotes the upstream(downstream) cell,  $N^W$  is the weighted counts,  $W$  is the weight used and  $N$  denotes the unweighted counts. The angles  $\Phi$ , in the modified double ratio, are the same used for the double ratio, Table 1.5, and give access to asymmetry amplitudes related to the same corresponding TMD functions. Under the same reasonable acceptance ratio assumption, Eq. 1.5, from the double ratio method the acceptance cancels out in the double ratio method. Using this assumption, the modified double ratio reduces to

$$R_{DM}^W(\Phi) \approx 2\tilde{D}_{\sin\Phi}\langle S_T \rangle A_T^{\sin(\Phi)W} \sin\Phi, \quad (1.13)$$

where  $\tilde{D}_{\sin\Phi}$  is an integrated depolarization factor defined as

$$\tilde{D}_{\sin\phi_S} = 1, \quad \tilde{D}_{\sin(2\phi \pm \phi_S)} = \frac{\int a(\theta) \sin^2 \theta d\cos\theta}{\int a(\theta)(1 + \cos^2\theta)d\cos\theta} = \frac{1 - \langle \cos^2\theta \rangle}{1 + \langle \cos^2\theta \rangle}. \quad (1.14)$$

The statistical error for the modified double ratio is

$$\sigma_{R_{DM}^W}^2 = \frac{\sum_{c,p} \sigma_{N_c^{pW}}^2 4(N_1^\uparrow N_2^\uparrow) N_1^\downarrow N_2^\downarrow)^2}{\sum_{c,p} \sigma_{N_c^p}^2 (N_1^\uparrow N_2^\uparrow + N_1^\downarrow N_2^\downarrow)^4} \sum_{c,p} \frac{1}{N_c^p}, \quad (1.15)$$

where  $\sigma_{N_c^{pW}}^2 = \sum(W_c^p)^2$  is the sum of event weights,  $c$  is cell 1 or cell 2 and  $p$  is polarization  $\uparrow$  or  $\downarrow$ .

The weighted asymmetry amplitude are determined by forming the modified double ratio in eight bins in the appropriate  $\Phi$  angle and fitting this distribution. If an infinite number of bins where used and there was sufficient data, the modified double ratio would be the function form of Eq. 1.13. Due to the limited statistics however,  $R_{DM}^W$  must be binned in a finite number of bins. Therefore to account for the fact that ratio is determined in a finite number of  $\Phi$  bins, the average value of Eq. 1.13 over the bin width is used as the fit distribution. This means the functional fit is

$$\langle R_{DM}^W \rangle = \frac{1}{\Delta\Phi} \int_{\Phi_i - \frac{\Delta\Phi}{2}}^{\Phi_i + \frac{\Delta\Phi}{2}} R_{DM}^W(\Phi') d\Phi' = \frac{2}{\Delta\Phi} \sin\left(\frac{\Delta\Phi}{2}\right) R_{DM}^W(\Phi_i), \quad (1.16)$$

where  $\Delta\Phi = \frac{2\pi}{8}$  for eight bins in  $\Phi$ . Fig. 1.11 shows the double ratio as a function of  $\Phi = \phi_S$  for period W07 in one bin of  $x_N$ . One  $R_{DM}^W$  is determined for each of the 3 (number of bins)  $\times$  9 (number of periods)  $\times$  3 (number of asymmetry amplitudes) = 81 modified double ratios.

#### 1.4.4 Results

As explained in Sec 1.3.2, the asymmetry amplitudes are determine for each period and the final asymmetry is determined as a period weighted average as in Eq. 1.10. For the same reason as the previous analyses and explained in Sec 1.3.2, the polarization and depolarization factors from each period are used to correct the asymmetry amplitude determined in each period. The final results are shown in Fig. 1.12 along with the results from the release values. As can be seen the results agree with those results obtained for the release which was a requirement before the results could be release to the public.

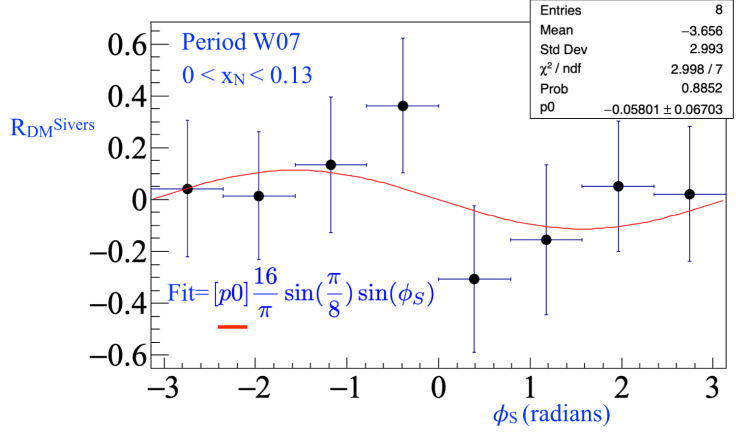


Figure 1.11: The double ratio as a function of  $\phi_S$  used to determine the Sivers asymmetry amplitude. This is for period W07 and the lowest bin in  $x_N$ . The red line shows the fit. The results of the fit are shown in the statistics box.

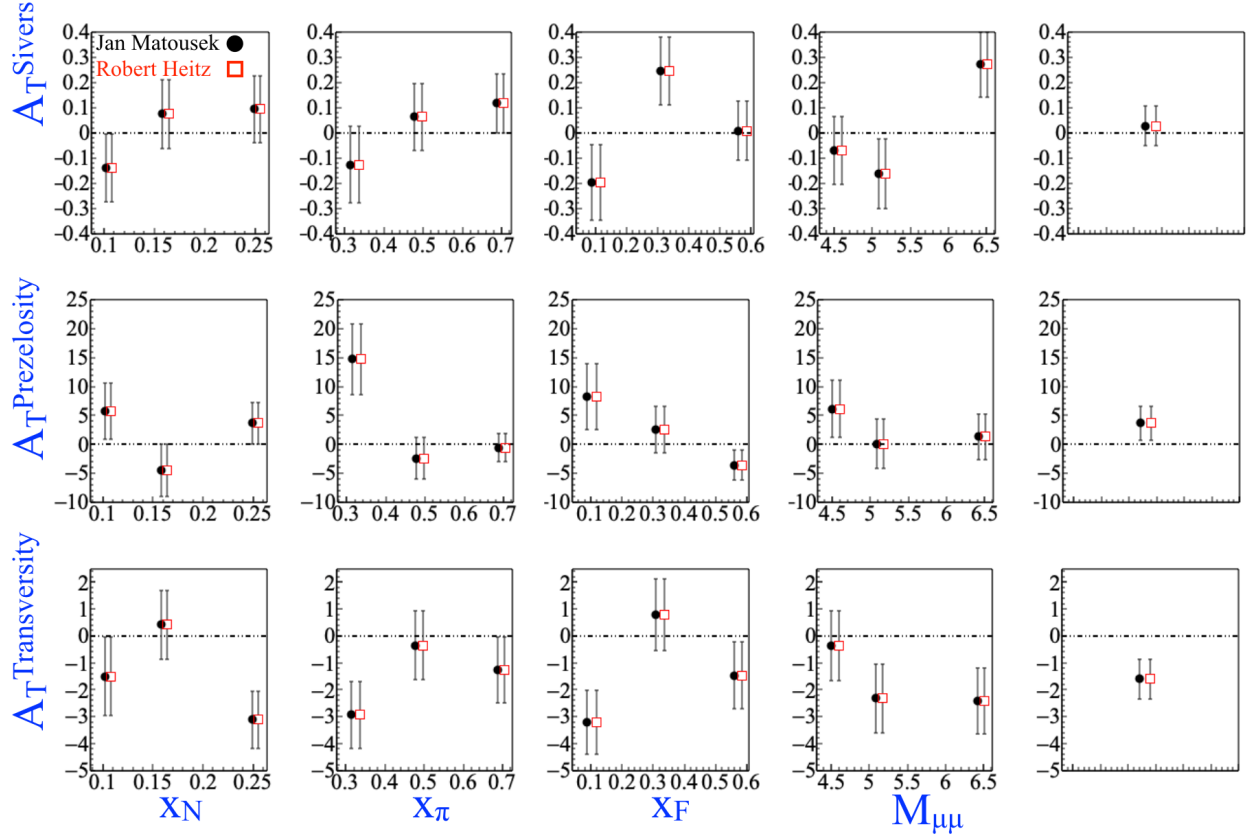


Figure 1.12: The comparison of weighted asymmetry amplitude results from the released values from Jan Matousek (black) and the cross checker Robert Heitz (red). From the top row down the asymmetry amplitudes are  $A_T^{\sin(\phi_S)q_T/M_N}$ ,  $A_T^{\sin(2\phi+\phi_S)q_T^3/(2M_\pi M_N^2)}$  and  $A_T^{\sin(2\phi-\phi_S)q_T/M_\pi}$  respectively.

## 1.5 Left-Right Asymmetries

This section goes over the analysis details for measuring the left-right asymmetry from the transversely polarized Drell-Yan data. A theoretical introduction showing how the left-right asymmetry is related to the Sivers TMD PDF and related past results for this asymmetry are given in Sec ???. In short the measured asymmetry can be defined as

$$A_{lr} = \frac{1}{|S_T|} \frac{\sigma_l - \sigma_r}{\sigma_l + \sigma_r}, \quad (1.17)$$

which when assuming the leading order Drell-Yan cross-section, Eq. ??, is related to the Sivers asymmetry amplitude as

$$A_{lr} = \frac{2A_T^{\sin(\phi_S)}}{\pi}. \quad (1.18)$$

There are many ways to determine the left-right asymmetry. The relevant techniques for the 2015 COMPASS setup are described and compared to ensure confidence of the end results.

### 1.5.1 Asymmetry Extractions

#### Geometric Mean

The most basic method to determine the left-right asymmetry is

$$A_{lr, simple} = \frac{1}{|S_T|} \frac{N_l - N_r}{N_l + N_r}, \quad (1.19)$$

where  $N_l = \int_{\phi_S=0}^{\phi_S=\pi} N(\phi_S) d\phi_S$  denotes the counts measure left and  $N_r = \int_{\phi_S=\pi}^{\phi_S=2\pi} N(\phi_S) d\phi_S$  denotes the counts measured right. Eq. 1.19 can be used to determine the left-right asymmetry per target cell. An intuitive picture of left and right defined in the target frame is shown in Fig. 1.13. This simple method to determine the left-right asymmetry is intuitive and can be helpful for visualizing the forthcoming methods to determine  $A_{lr}$ . Left and right in all definitions in this section are determined relative to the target spin direction as

$$\begin{aligned} \text{Left} : & \hat{q}_T \cdot (\hat{S}_T \times \hat{P}_\pi) > 0 \\ \text{Right} : & \hat{q}_T \cdot (\hat{S}_T \times \hat{P}_\pi) < 0, \end{aligned} \quad (1.20)$$

where  $\hat{q}_T$ ,  $\hat{S}_T$  and  $\hat{P}_\pi$  are unit vectors in the target reference frame for the virtual photon transverse momentum, the target spin and the beam pion momentum respectively.

The simple definition of the left-right asymmetry, Eq. 1.19, is unfortunately dependent on the spectrom-

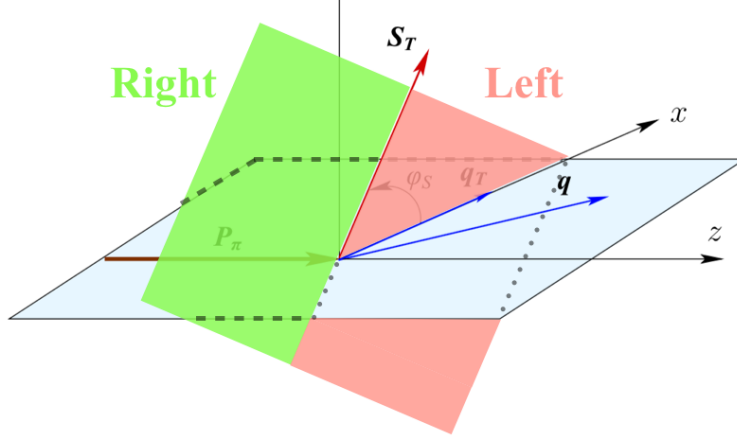


Figure 1.13: The definition of the left plane (red) and right plane (green) defined from a target spin up configuration in the target frame

eter acceptance. This is can be realized from the fact that the definition of the detected counts, Eq. 1.2, depends on the spectrometer acceptance  $a(\phi_S)$  which therefore means  $A_{lr,simple}$  also depends on the spectrometer acceptance. This is a problem because the spectrometer acceptance can change with time and space and therefore can be dependent on the physical kinematics which produced the event. Such dependencies can cause unphysical false asymmetries in the measurement of  $A_{lr}$  and must therefore be removed or must be included as systematic effects.

Forming the geometric mean asymmetry is a way to determine the left-right asymmetry without acceptance effects from the spectrometer. The geometric mean asymmetry is defined as

$$A_{lr,geo} = \frac{1}{|S_T|} \frac{\sqrt{N_l^\uparrow N_r^\downarrow} - \sqrt{N_r^\uparrow N_l^\downarrow}}{\sqrt{N_l^\uparrow N_l^\downarrow} + \sqrt{N_r^\uparrow N_r^\downarrow}}, \quad (1.21)$$

which also defines a left-right asymmetry per target cell. It is not difficult to simplify the geometric mean asymmetry as

$$A_{lr,geo} = \frac{1}{|S_T|} \frac{\kappa_{geo} \sqrt{\sigma_l \sigma_l} - \sqrt{\sigma_r \sigma_r}}{\kappa_{geo} \sqrt{\sigma_l \sigma_l} + \sqrt{\sigma_r \sigma_r}} = \frac{1}{|S_T|} \frac{\kappa_{geo} \sigma_l - \sigma_r}{\kappa_{geo} \sigma_l + \sigma_r}, \quad (1.22)$$

where  $\kappa_{geo}$  is a ratio of acceptances defined for the geometric mean as

$$\kappa_{geo} = \frac{\sqrt{a_J^\uparrow a_S^\downarrow}}{\sqrt{a_S^\uparrow a_J^\downarrow}}, \quad (1.23)$$

where  $J$  stands for the Jura spectrometer side and  $S$  stands for Saleve spectrometer side which are the west and east sides respectively. The assumption made for the notation in Eq. 1.23, which will be made

throughout this section, is that the target is polarized exactly vertical in the target frame. If this assumption violated, the Jura and Saleve acceptances blend into each other and Eq. 1.23 is no longer the correct notation for the acceptance ratio. The assumption is violated when the beam particle and the target polarization do not make a right angle in the laboratory frame, in which case the target will no longer be polarized vertically in the target frame. However the target will be assumption to be vertically polarized in the target frame strictly for ease of notation.

Relation 1.22 is equal to  $A_{lr}$  if  $\kappa_{geo} = 1$ . However as stated previously, time effects can vary  $\kappa_{geo}$  from unity. These effects are estimated through false asymmetry analysis and included in the systematic error bars described in Sec 1.5.2. Equation 1.21 is therefore to a good approximation an acceptance free method to determine  $A_{lr}$ . It is also defined for the upstream and downstream cells independently and therefore can be used as a consistency check between the two target cells.

The statistical uncertainty of the geometry mean is

$$\delta A_{lr,geo} = \frac{1}{|S_T|} \frac{\sqrt{N_l^\uparrow N_l^\downarrow N_r^\uparrow N_r^\downarrow}}{\left(\sqrt{N_l^\uparrow N_l^\downarrow} + \sqrt{N_r^\uparrow N_r^\downarrow}\right)^2} \sqrt{\frac{1}{N_l^\uparrow} + \frac{1}{N_l^\downarrow} + \frac{1}{N_r^\uparrow} + \frac{1}{N_r^\downarrow}} , \quad (1.24)$$

which reduces to  $\frac{1}{|S_T|} \frac{1}{\sqrt{N}}$ , where  $N = N_l^\uparrow + N_l^\downarrow + N_r^\uparrow + N_r^\downarrow$ , in the case of equal statistics per target cell meaning  $N_l^\uparrow = N_l^\downarrow = N_r^\uparrow = N_r^\downarrow = N/4$

## Two-Target Geometric Mean

The previous geometric mean asymmetry determined an  $A_{lr}$  per target cell. As described in Sec 1.1 however, COMPASS had two oppositely polarized target cells in 2015. It is desirable from a statistical point of view and for comparison purposes to determine one  $A_{lr}$  from the 2015 COMPASS setup. This can be accomplished by modifying the geometric mean to add both target cells as follows

$$A_{lr,2Targ} = \frac{1}{|S_T|} \frac{\sqrt[4]{N_{1,l}^\uparrow N_{1,l}^\downarrow N_{2,l}^\uparrow N_{2,l}^\downarrow} - \sqrt[4]{N_{1,r}^\uparrow N_{1,r}^\downarrow N_{2,r}^\uparrow N_{2,r}^\downarrow}}{\sqrt[4]{N_{1,l}^\uparrow N_{1,l}^\downarrow N_{2,l}^\uparrow N_{2,l}^\downarrow} + \sqrt[4]{N_{1,r}^\uparrow N_{1,r}^\downarrow N_{2,r}^\uparrow N_{2,r}^\downarrow}} . \quad (1.25)$$

As in the basic geometric mean asymmetry, Sec 1.5.1, left and right are determined relative to the spin direction of the target as in Eq. 1.20. Similarly to Eq. 1.22, the two-target geometric mean asymmetry can be written as

$$A_{lr,2Targ} = \frac{1}{|S_T|} \frac{\kappa_{2Targ} \sqrt[4]{\sigma_l \sigma_l \sigma_l \sigma_l} - \sqrt[4]{\sigma_r \sigma_r \sigma_r \sigma_r}}{\kappa_{2Targ} \sqrt[4]{\sigma_l \sigma_l \sigma_l \sigma_l} + \sqrt[4]{\sigma_r \sigma_r \sigma_r \sigma_r}} = \frac{1}{|S_T|} \frac{\kappa_{2Targ} \sigma_l - \sigma_r}{\kappa_{2Targ} \sigma_l + \sigma_r} , \quad (1.26)$$

,

where now  $\kappa_{2Targ}$  is the ratio of acceptances from all targets and polarizations. This inclusive acceptance ratio is defined as

$$\kappa_{2Targ} = \frac{\sqrt[4]{a_{1,J}^{\uparrow} a_{1,S}^{\downarrow} a_{2,J}^{\uparrow} a_{2,S}^{\downarrow}}}{\sqrt[4]{a_{1,S}^{\uparrow} a_{1,J}^{\downarrow} a_{2,S}^{\uparrow} a_{2,J}^{\downarrow}}}. \quad (1.27)$$

In this case the acceptance ratio is expected to vary less with time and therefore be closer to unity than the normal geometric mean acceptance ratio, Eq. 1.23. This is a consequence of having the different target cells oppositely polarized. Rewriting Eq. 1.27 with sub-period superscripts instead of target polarization superscripts results in the equation

$$\kappa_{2Targ} = \frac{\sqrt[4]{a_{1,J}^{one} a_{1,S}^{two} a_{2,J}^{two} a_{2,S}^{one}}}{\sqrt[4]{a_{1,S}^{one} a_{1,J}^{two} a_{2,S}^{two} a_{2,J}^{one}}} \quad (1.28)$$

where sub-period *one* is with the upstream target polarized up and the downstream target polarized down and vice versa for sub-period *two*. From Eq. 1.28 it is more evident that the acceptance ratio terms for sub-period *two* are reciprocal to the terms for sub-period *one* and therefore the acceptance ratio is expected to be more stably close to unity.

Finally the statistical uncertainty of the two target geometric mean is

$$\delta A_{lr,2Targ} = \frac{1}{|S_T|} \frac{LR}{(L+R)^2} \sqrt{\sum_{c,p} \left( \frac{1}{N_L^p} + \frac{1}{N_R^p} \right)} \quad , \quad (1.29)$$

where  $L$  can be thought of as the left counts and equals to  $\sqrt[4]{N_{1,L}^{\uparrow} N_{1,L}^{\downarrow} N_{2,L}^{\uparrow} N_{2,L}^{\downarrow}}$  and  $R$  can be thought of as the right counts and equals to  $\sqrt[4]{N_{1,R}^{\uparrow} N_{1,R}^{\downarrow} N_{2,R}^{\uparrow} N_{2,R}^{\downarrow}}$ . As with the geometric mean asymmetry, in the case of equal statistic populations in each direction and target polarization, the statistical uncertainty for the two-target geometric mean also reduces to  $\frac{1}{|S_T|} \frac{1}{\sqrt{N}}$ , where  $N$  is the sum of all counts.

### 1.5.2 Systematic Studies

Several tests were performed to estimate the systematic uncertainty of the left-right asymmetry. The systematic errors are determined by adding all non-zero systematic uncertainties in quadrature. The impact from each source of systematic error is summarized in Tab. 1.8.

#### Period Compatibility (Time Dependence)

The asymmetries calculated for each time period in each kinematic bin are shown in Fig. 1.14.

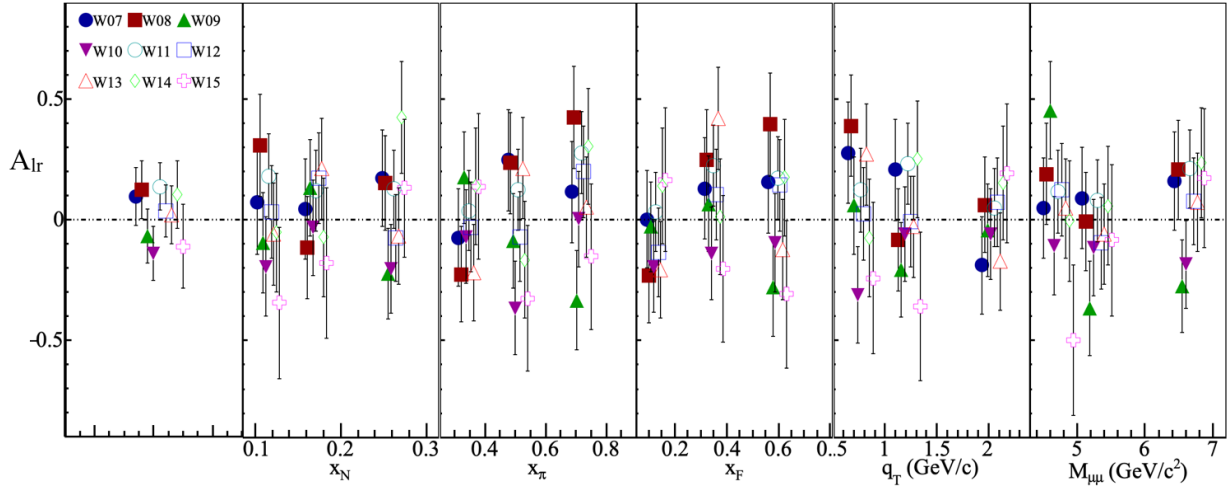


Figure 1.14:  $A_{lr}$  determined for each period

By eye the asymmetry fluctuations appear to be statistically compatible. To quantify the compatibility of the asymmetries between the periods, a pull distribution is formed where the pull value is defined as

$$\Delta A_i = \frac{A_i - \langle A \rangle}{\sqrt{\sigma_{A_i}^2 - \sigma_{\langle A \rangle}^2}}, \quad (1.30)$$

and is determined for each period and kinematic bin. There are therefore 3 (number of bins)  $\times$  5 (number of kinematics)  $\times$  9 (number of periods) = 135 entries in the pull distribution. The pull distribution is shown in Fig. 1.15 along with a Gaussian fit to determine the distributions width and average. If the asymmetries all come from the same parent distribution then, due to the central limit theorem, the pull distribution will be a Gaussian distribution with zero mean and unit variance. The discrepancy of the pull distribution from a standard Gaussian distribution is used to determine a systematic error as

$$\frac{\sigma_{\text{systematic}}}{\sigma_{\text{statistical}}} = \sqrt{|\sigma_{\text{pull}}^2 - 1|} + \frac{\mu_{\text{pull}}}{2}. \quad (1.31)$$

As the asymmetries in different kinematic bins are formed using the same data set, the asymmetries between kinematic binnings are correlated. For this reason an uncorrelated pull distribution is also formed for each kinematic bin and also compared with a standard Gaussian distribution. These distributions are shown in Fig. 1.16 along with the results of their respective Gaussian fits. For these uncorrelated pull distributions there are now only 3 (number of bins)  $\times$  9 (number of periods) = 27 entries in each kinetically binned pull distributions and only 9 (number of periods) bins in the integrated pull distribution.

Even though the Gaussian fits did not give exactly a standard Gaussian, the fit parameters are well

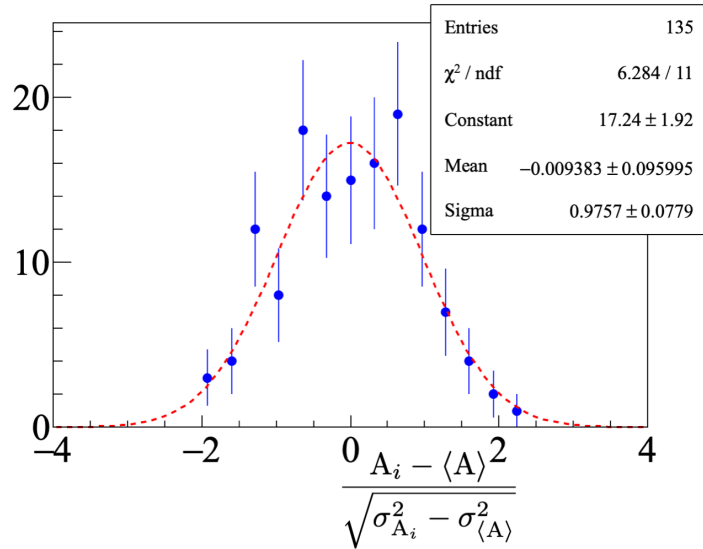


Figure 1.15: Pull distribution from the two-target geometric mean

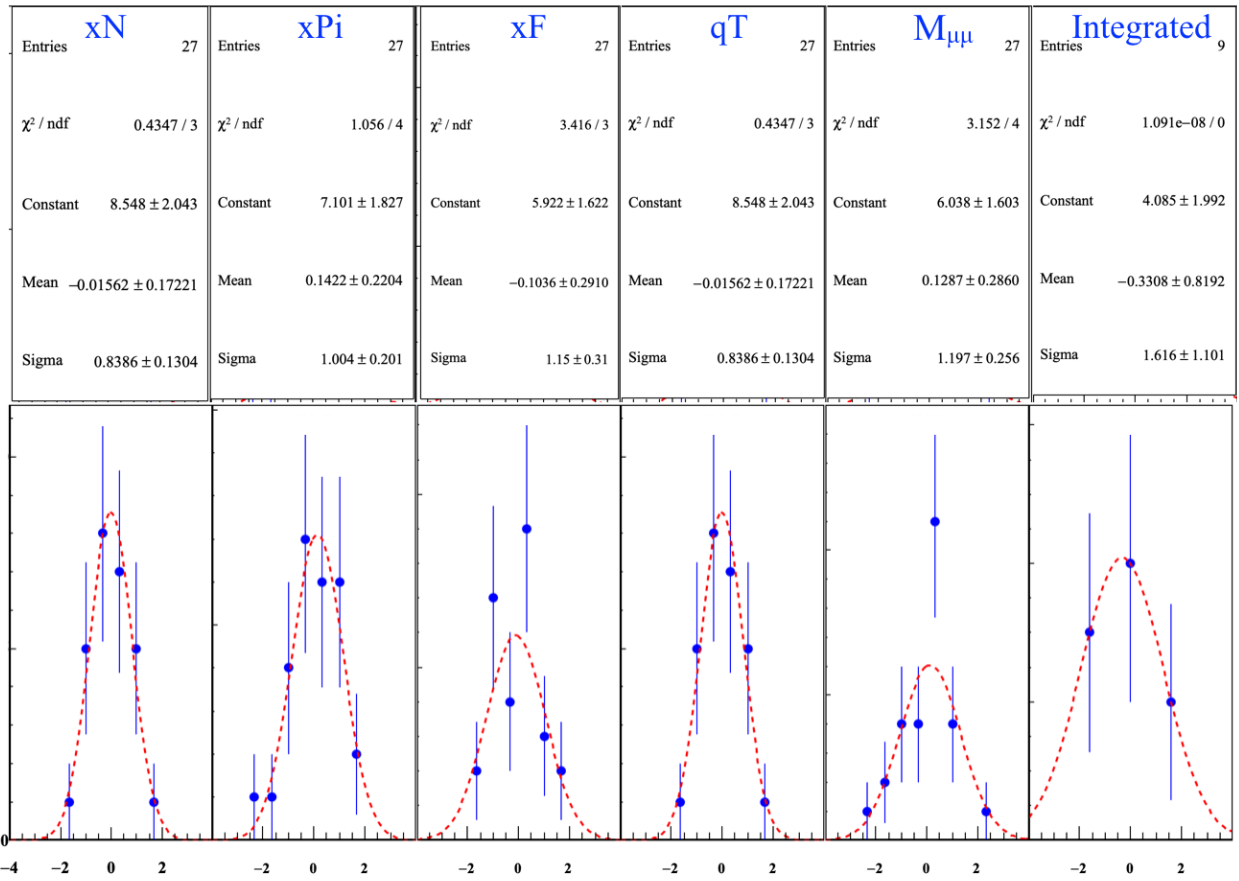


Figure 1.16: Uncorrelated pull distributions and Results of the Gaussian fit for the pull distributions

compatible with a standard Gaussian within the errors of the fit. Therefore no systematic error was assigned due to incompatibility of the periods.

### Left/Right Event Migration

The spectrometer has finite resolution for any measured quantity. For this reason events measured as left outgoing could really be events that are right outgoing and vice versa. This left-right misidentification has the result of diluting spin-dependent effects by effectively having a sample from an unpolarized target along with the sample from the polarized target. Therefore the asymmetry  $A_{lr}$  reduces from left-right misidentification and this effect is included as a systematic effect.

A Monte-Carlo data set was analyzed to determine the left-right misidentification percentage. Four Monte-Carlo processes were generated corresponding to three background processes and a spin-independent signal process. The generator used was PHTHYIA8 and the data was generated and reconstruction at Blue Waters. The background processes simulated were JPsi production, Psi' production and open charm (OC) production. Each of these backgrounds can decay into two muons which results in a background contamination to the Drell-Yan signal. Table 1.6 gives the parameters used for the Monte-Carlo generated.

Table 1.6: Monte-Carlo settings produced on Blue Waters

Description	Monte-Carlo Setting	Setting
Event generator	PYTHIA8	
Pion PDF	GRVPII	
Proton PDF	NNPDF23	
Proton/Neutron mixing ratio	1.96	
Initial state radiation	on	
Final state radiation	on	
Multiple parton interactions	on	
GEANT4 detector simulation	TGEANT	
Simulated detector efficiency distributions	uniform	

The generated Monte-Carlo data corresponds to a  $4\pi$  spectrometer acceptance. The COMPASS spectrometer on the other hand, does not have a full  $4\pi$  acceptance. Therefore to produce simulated data that corresponds to the actual data taking conditions, a GEANT4 [6] based detector simulation, called TGEANT [7], simulated the COMPASS spectrometer response to the generated data. The data from TGEANT was then reconstructed with the same reconstruction software as real data.

Misidentification was estimated by comparing the data input to TGEANT with the output reconstructed data. The same analysis and cuts were performed on the simulated and then reconstructed data as were performed on the real data set. Fig. 1.17 shows the rate of events identified correctly and incorrectly as a function of  $\phi_S$ . Fig. 1.17 is made by comparing which outgoing direction the generated events emerged with

the outgoing direction the reconstructed events emerged.

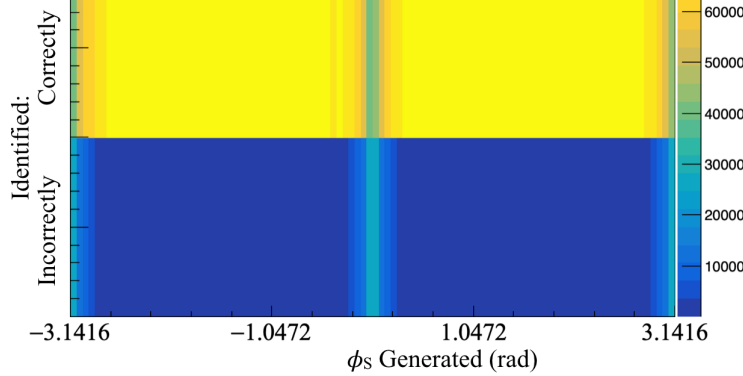


Figure 1.17: The rate of identified correctly and incorrectly left-right events as a function of  $\phi_S$ . This is determined by comparing the generated outgoing direction with the reconstructed outgoing direction. The left-right boundary is clearly visible at  $\phi_S = 0$  rad and  $\phi_S = -\pi$  rad and  $\phi_S = \pi$  rad

As is clearly visible in Fig. 1.17, there is a band of higher misidentification rate at the border between left and right. For this reason a cut on the  $\phi_S$  variable symmetric about the left-right border was tested to determine the percent of misidentification as a function of the amount of  $\phi_S$  cut. These results are shown in Fig. 1.18.

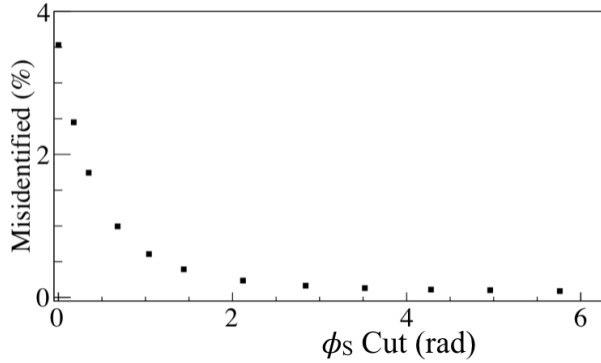


Figure 1.18: Percent left-right migration as a function of the amount of  $\phi_S$  cut.

The systematic error for left-right migration is calculated as

$$\delta A_{N,\text{systematic}} = \gamma * A_N + \gamma * \delta A_N, \quad (1.32)$$

where this expression is derived in Appendix A.2. No cut on  $\phi_S$  was ultimately used for the asymmetry determination. This is to avoid loss of statistics and due to the fact that the systematic error is already small with no cut in  $\phi_S$ . The integrated systematic error due to left-right event migration was determined to be 9%.

## False Asymmetries

### Acceptance From False Asymmetries

As was pointed out in Sec. 1.5.1 and Sec. 1.5.1, the asymmetry measurement assumes the acceptance does not change with time and therefore the acceptance ratio,  $\kappa$  is unitary. Any deviation from a unitary acceptance ratio is estimated with a false asymmetry and is taken as a systematic error. To determine if acceptance does change with time, a false asymmetry is calculated where the only way the false asymmetry could be non-zero is if acceptance changes with time. This false asymmetry for the two-target geometric mean is

$$\begin{aligned} A_{lr, \text{False}} &= \frac{1}{|S_T|} \frac{\sqrt[4]{N_{1,r}^{\uparrow} N_{1,l}^{\downarrow} N_{2,l}^{\uparrow} N_{2,r}^{\downarrow}} - \sqrt[4]{N_{1,l}^{\uparrow} N_{1,r}^{\downarrow} N_{2,r}^{\uparrow} N_{2,l}^{\downarrow}}}{\sqrt[4]{N_{1,r}^{\uparrow} N_{1,l}^{\downarrow} N_{2,l}^{\uparrow} N_{2,r}^{\downarrow}} + \sqrt[4]{N_{1,l}^{\uparrow} N_{1,r}^{\downarrow} N_{2,r}^{\uparrow} N_{2,l}^{\downarrow}}} \\ &= \frac{1}{|S_T|} \frac{\alpha_{2Targ} \sqrt[4]{\sigma_r \sigma_l \sigma_l \sigma_r} - \sqrt[4]{\sigma_l \sigma_r \sigma_r \sigma_l}}{\alpha_{2Targ} \sqrt[4]{\sigma_r \sigma_l \sigma_l \sigma_r} + \sqrt[4]{\sigma_l \sigma_r \sigma_r \sigma_l}} = \frac{1}{|S_T|} \frac{\alpha_{2Targ} - 1}{\alpha_{2Targ} + 1}, \end{aligned} \quad (1.33)$$

where  $\alpha_{2Targ}$  is an acceptance ratio and is defined as

$$\alpha_{2Targ} = \frac{\sqrt[4]{a_{1,S}^{\uparrow} a_{1,S}^{\downarrow} a_{2,J}^{\uparrow} a_{2,J}^{\downarrow}}}{\sqrt[4]{a_{1,J}^{\uparrow} a_{1,J}^{\downarrow} a_{2,S}^{\uparrow} a_{2,S}^{\downarrow}}}. \quad (1.34)$$

The false asymmetry, Eq. 1.33, can be simplified as

$$A_{lr, \text{False}} = \frac{1}{|S_T|} \frac{\sqrt[4]{N_{1,S} N_{2,J}} - \sqrt[4]{N_{1,J} N_{2,S}}}{\sqrt[4]{N_{1,S} N_{2,J}} + \sqrt[4]{N_{1,J} N_{2,S}}}. \quad (1.35)$$

That is  $A_{lr, \text{False}}$  is the normalized difference of counts from each target cell assuming the upstream target is always polarized down and the downstream target is always polarized up. Given that the polarization flips for both upstream and downstream target cells,  $A_{lr, \text{False}}$  is an asymmetry where physical effects cancel out. The kinematic dependencies of the false asymmetry are shown in Fig. 1.19 and the kinematic dependencies of the acceptance ratio,  $\alpha_{2Targ}$ , are shown in Fig. 1.20.

While  $\alpha_{2Targ}$  is an acceptance ratio it is not the same as,  $\kappa_{2Targ}$  the acceptance ratio in the true asymmetry. However  $\alpha_{2Targ}$  is similar to  $\kappa_{2Targ}$  in that  $\alpha_{2Targ}$  will only be different from unity as a result of time changes in the spectrometer. Therefore it is assumed  $\alpha_{2Targ}$  can be used as a good estimate of the true acceptance ratio fluctuations. The systematic error due to acceptance fluctuations is determined as

$$\delta A_{lr, \text{systematic}} = \frac{1}{|S_T|} \left( \frac{|\alpha_{2Targ} - 1|}{2} + \delta_{\frac{|\alpha_{2Targ} - 1|}{2}} \right), \quad (1.36)$$

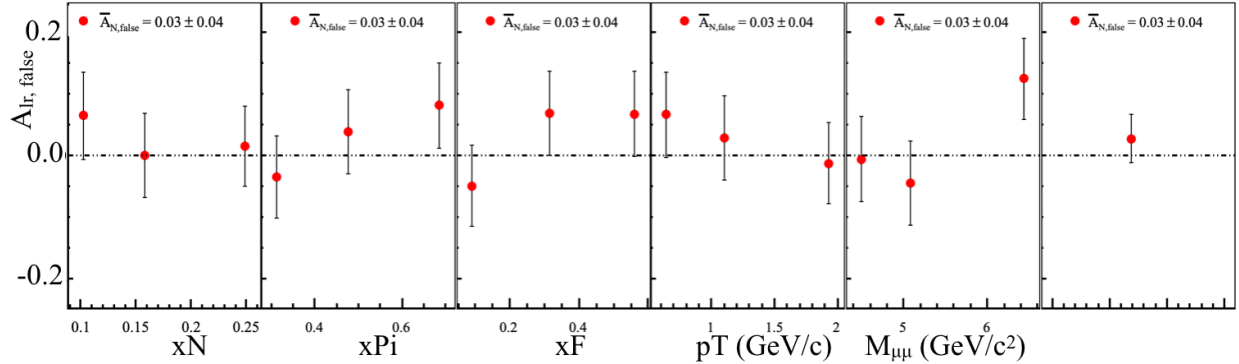


Figure 1.19: False asymmetry,  $A_{lr, False}$ , to estimate fluctuations in acceptance in time

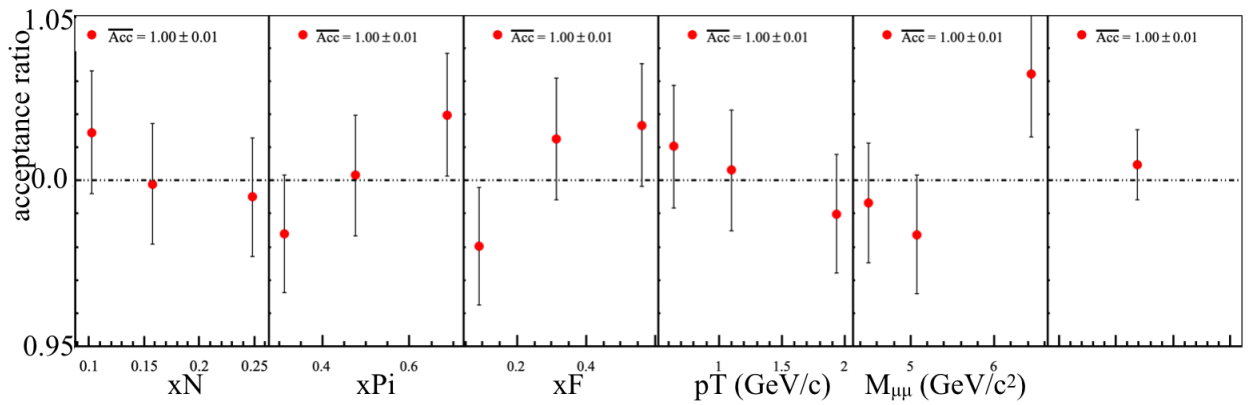


Figure 1.20: Acceptance ratio  $\alpha_{2Targ}$ , Eq. 1.34, used to determine the systematic effects from acceptance changes in time

where this expression is derived in Appendix A.1. The kinematic dependence of the systematic error normalized to the statistical error is shown in Fig. 1.21. The binned average systematic error due to acceptance is 20% of the statistical error.

### Further False Asymmetry Effects

Although the list of systematic effects specifically studied is quite exhaustive there is always the potential for other systematic effects not considered. Studies of the changes in time from additional false asymmetries were performed in an attempt to take into account all other systematic effects. All false asymmetries considered must be constructed in such a way that the physical process of interest cancels out. A false asymmetry could therefore only be non-zero from acceptance effects, luminosity or some other reason not considered. The additional false asymmetries are constructed in a way that luminosity effects cancel out and acceptance effects are approximately constant. With these assumptions, the pull values from Eq. 1.30

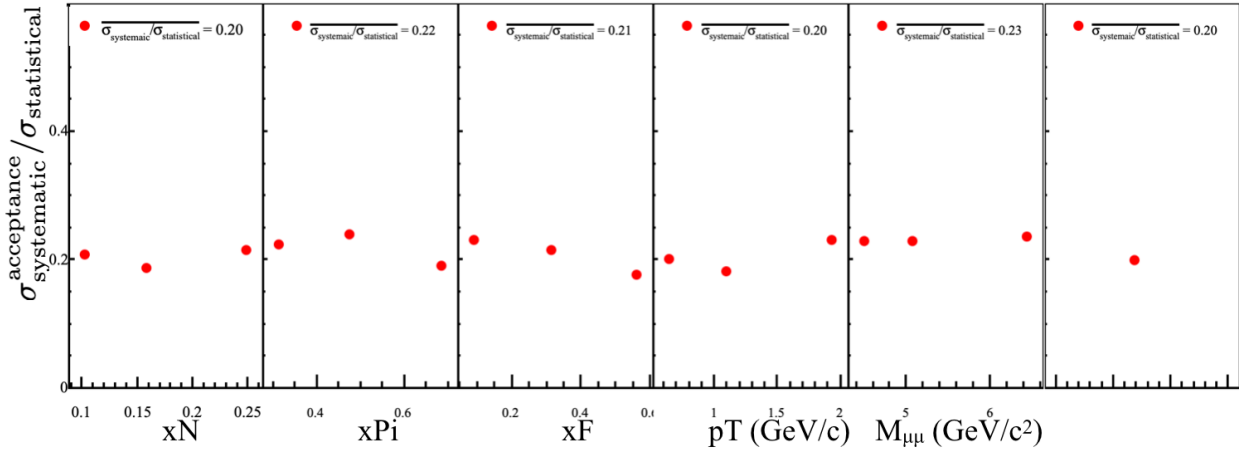


Figure 1.21: Systematic error due to acceptance effects

are expected to be distributed as a standard Gaussian distribution. Any deviation from a standard Gaussian is conservatively taken as a systematic effect from some unknown cause. The additional studied false asymmetries are summarized in the following enumerated list.

1. A false asymmetry similar to Eq. 1.33 but with the upstream left and right counts flipped defined as

$$A_{lr,F1} = \frac{1}{|S_T|} \frac{\sqrt[4]{N_{1,l}^\uparrow N_{1,r}^\downarrow N_{2,l}^\uparrow N_{2,r}^\downarrow} - \sqrt[4]{N_{1,r}^\uparrow N_{1,l}^\downarrow N_{2,l}^\uparrow N_{2,r}^\downarrow}}{\sqrt[4]{N_{1,l}^\uparrow N_{1,r}^\downarrow N_{2,l}^\uparrow N_{2,r}^\downarrow} + \sqrt[4]{N_{1,r}^\uparrow N_{1,l}^\downarrow N_{2,l}^\uparrow N_{2,r}^\downarrow}}. \quad (1.37)$$

This false asymmetry can be thought of as measuring the normalized counts on the Jura side minus the Saleve side. The period weighted average results of this false asymmetry are shown in Fig. 1.22. As Fig. 1.22 shows, the asymmetry is systematically less than zero by more than a standard deviation resulting from acceptance effects. The uncorrelated pull distributions from this false asymmetry are shown in Fig. 1.23 along with the corresponding Gaussian fit results. Due to the fact that there are less entries in these pull distributions the Gaussian fit results are not necessarily that good. In an attempt to correct for this and to take into account the fit errors, a weighted average of the mean and standard deviation are made, as in Eq. 1.10, using weights as the inverse fit variances. The resulting systematic error is again determined as in Eq. 1.31 using the weighted mean and weighted standard deviation.

2. A false asymmetries using only the information from the upstream or the downstream target defined as

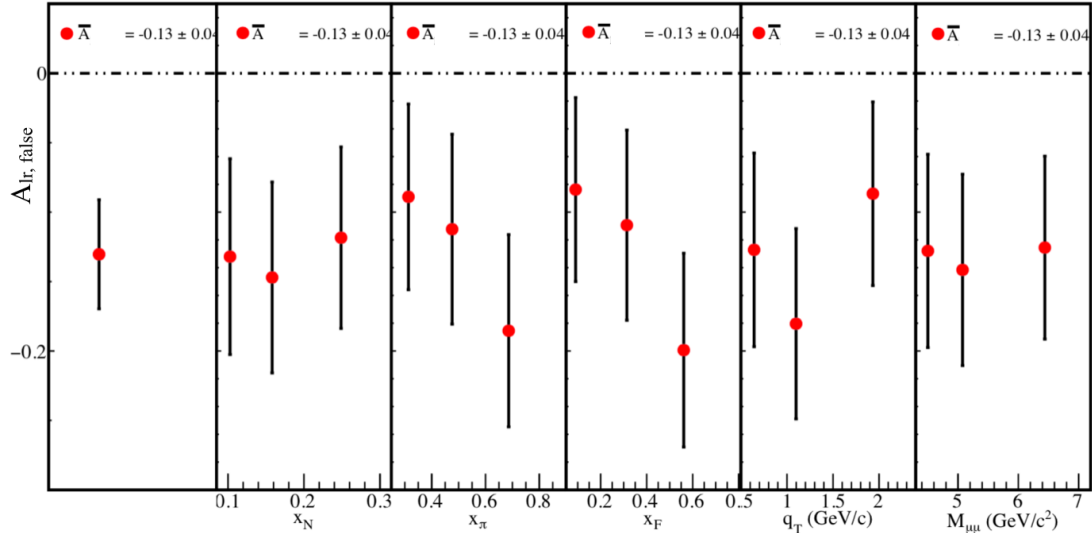


Figure 1.22: Two-target geomean false asymmetry. This is non-zero due to acceptance effects

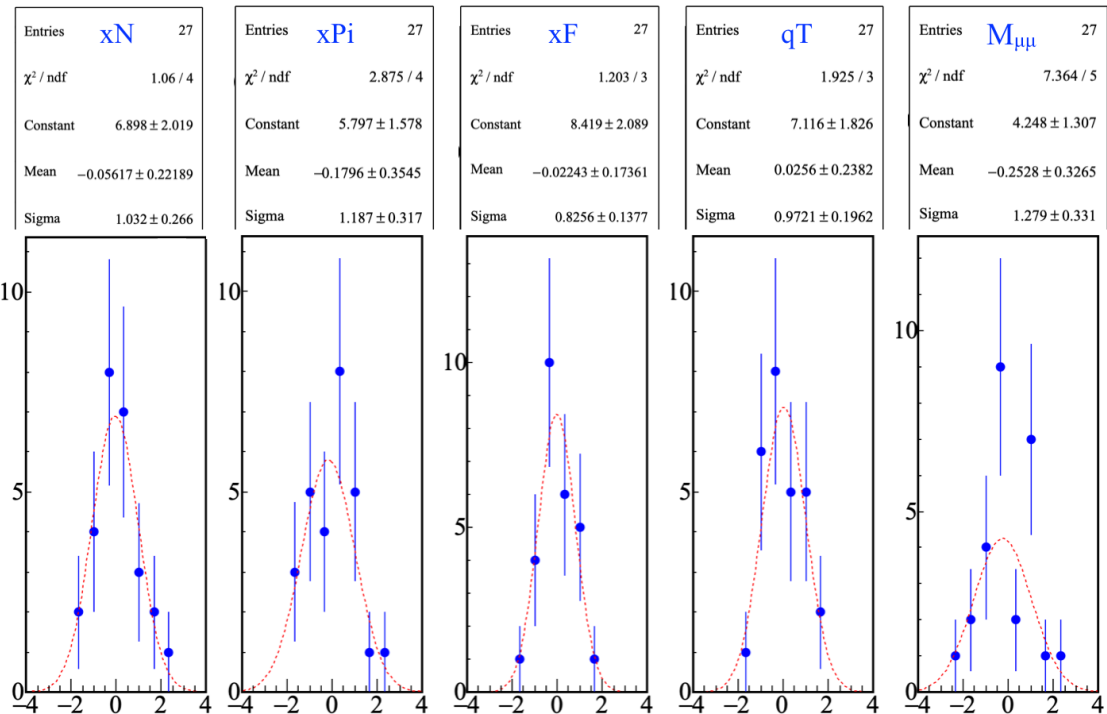


Figure 1.23: Uncorrelated pulls of the two-target geomean false asymmetry and Gaussian fit results

$$A_{lr,F2} = \frac{1}{|S_T|} \frac{\sqrt{N_l^\uparrow N_r^\downarrow} - \sqrt{N_r^\uparrow N_l^\downarrow}}{\sqrt{N_l^\uparrow N_r^\downarrow} + \sqrt{N_r^\uparrow N_l^\downarrow}}. \quad (1.38)$$

This false asymmetry can also be thought of as measuring the normalized counts on the Jura side

minus the Saleve side but for each target individually. Both this false asymmetry and the previous false asymmetry, Eq. 1.37, can be written as

$$A_{lr,F1/2} = \frac{1}{|S_T|} \frac{\alpha - 1}{\alpha + 1} \quad (1.39)$$

where  $\alpha$  will be an acceptance ratio of Jura/Saleve. As the Jura/Saleve acceptance ratio is expected to be the same for the upstream and downstream targets, any difference between the two false asymmetries must be due to other reasons. A by period comparison between the upstream and downstream target is shown in Fig. 1.24 and as can be seen there are differences by period between the upstream and downstream asymmetries. A combined pull distribution is made using the information from both upstream and downstream asymmetries and is shown in Fig. 1.25. As with the previous false asymmetry, lack of data leads to the same problems with fit and therefore the same weighting method is used to determine a systematic error.

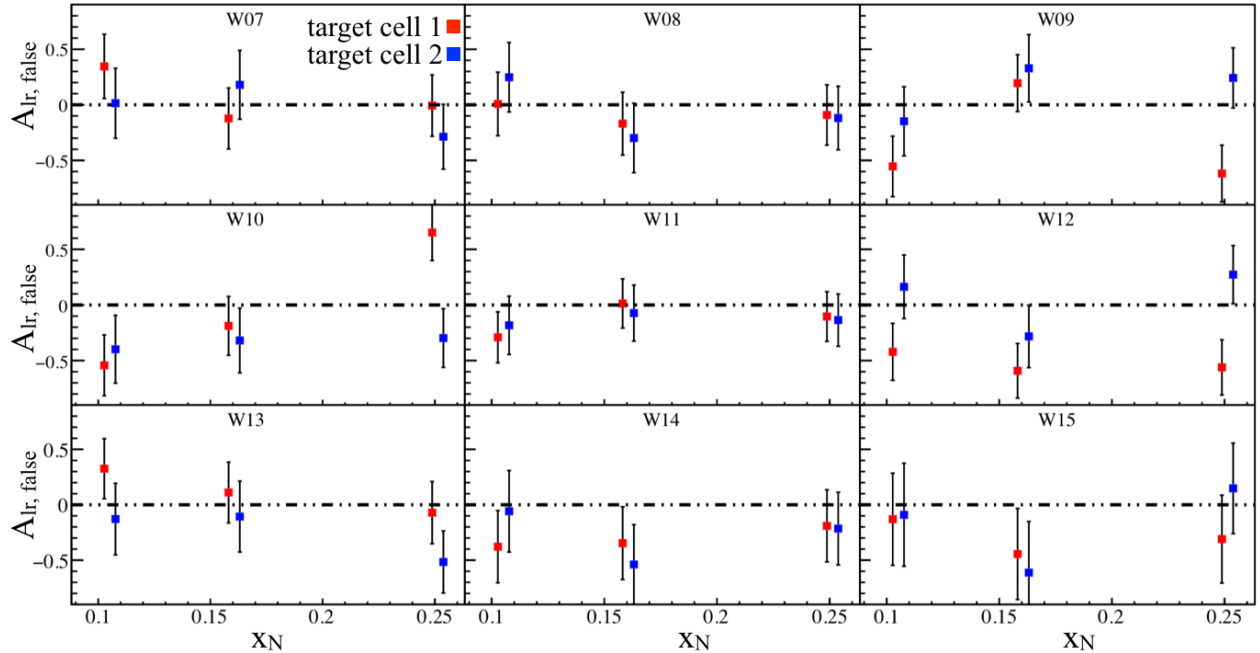


Figure 1.24: One target false asymmetries for the upstream target (red) and the downstream target (blue), as a function of  $x_N$ . Each graph is from a different period in time.

3. Finally the same false asymmetry used to determine the acceptance fluctuations, Eq. 1.33, is also checked for compatibility and a systematic error is determined in the same way as the previous false asymmetries. The pulls are shown in Fig. 1.26 along with the corresponding fit parameters and errors.

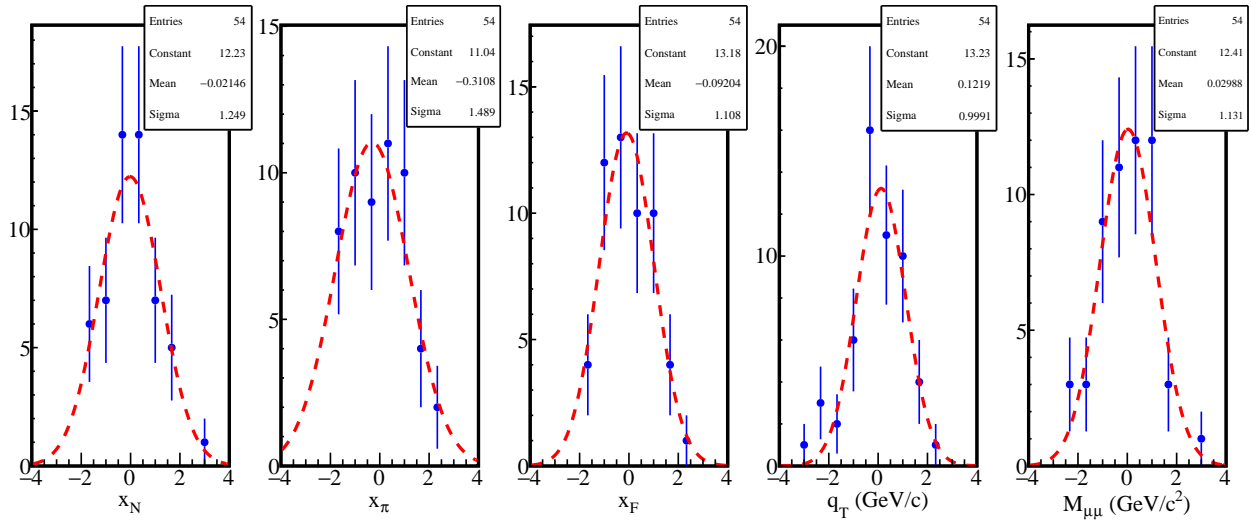


Figure 1.25: Pull values from one-target geommean false asymmetries. Both upstream and downstream values are used to make this pull

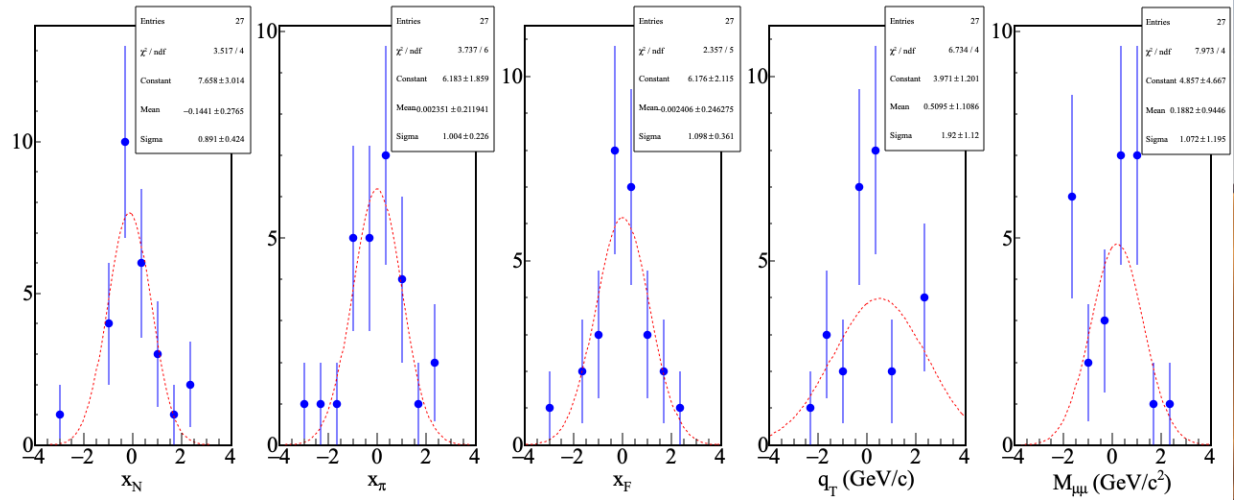


Figure 1.26: Pull distribution for a nearly acceptance free two-target false geommean asymmetry

A summary of the systematic error from each false asymmetry is shown in Tab. 1.7

Systematic error	$\langle \sigma_{\text{systematic}} / \sigma_{\text{statistical}} \rangle$
Two target Jura-Saleve	0.26
Combined one target	0.5
Two target acceptance estimation	0.29

Table 1.7: Summary of systematic error impacts from false asymmetries. The maximum systematic error is chosen as the systematic error.

## Total Systematics

The total systematic error is determined by adding all non-zero systematic effects in quadrature as

$$\left\langle \frac{\sigma_{\text{systematic}}}{\sigma_{\text{statistical}}} \right\rangle = \sqrt{\sum_i^{\text{all systematic}} \left\langle \frac{\sigma_{\text{systematic},i}^2}{\sigma_{\text{statistical}}^2} \right\rangle}, \quad (1.40)$$

where all the systematic effects considered are summarized in Tab. 1.8. For reference the total statistical error is  $\langle \sigma_{\text{statistical}} \rangle = 0.039$ .

Systematic error	$\langle \sigma_{\text{systematic}}/\sigma_{\text{statistical}} \rangle$	$\langle \sigma_{\text{systematic}} \rangle$
Period compatibility	0.0	0.0
Left-Right migration	0.09	0.004
Target Polarization	0.05	0.003
Dilution Factor	0.05	0.003
Acceptance fluctuation	0.2	0.008
False asymmetry	0.5	0.020
<b>Total</b>	<b>0.55</b>	<b>0.022</b>

Table 1.8: Summary of systematic error impacts to the integrated asymmetry

### 1.5.3 Results

The left-right asymmetry is extracted per period, corrected for the target polarization and ultimately combined as a weighed average, Eq. 1.10, to get an overall result as in Sec 1.3.2.

The results for the geometric mean are shown in Fig. 1.27 and the results for the two-target geometric mean are shown in Fig. 1.28. The numerical values for the two-target geometric mean systematic errors are summarized in Table 1.8.

It was shown in Sec ?? that the left-right asymmetry is related to the Sivers amplitude as

$$A_{lr} = \frac{2A^{\sin(\phi_S)}}{\pi} = \frac{2A_N}{\pi}, \quad (1.41)$$

where  $A_N$  is the analyzing power. The Sivers amplitude was measured to be approximately 1 sigma above zero from the unbinned maximum likelihood method, Fig. 1.6, the double ratio method, Fig. 1.8, and the left-right asymmetry. Adjusting the left-right asymmetry, as in Eq. 1.41, shows the amplitude determined from the left-right asymmetry is statistically consistent with the Sivers amplitude determined from the double ratio method, Fig. 1.29. Therefore all methods to determine the Siver amplitude in this chapter are consistent with the sign flip hypothesis between the Drell-Yan and SIDIS processes. On the other hand, the

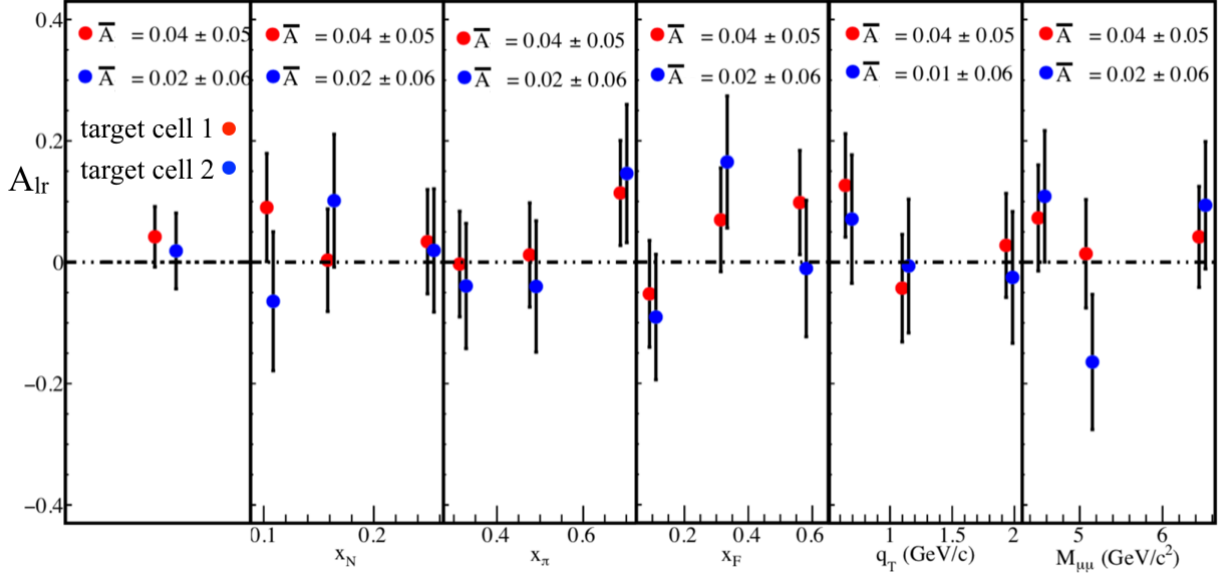


Figure 1.27:  $A_{lr}$  determined from the geometric mean method for the upstream target cell (red) and the downstream target cell (blue) for all kinematic binnings

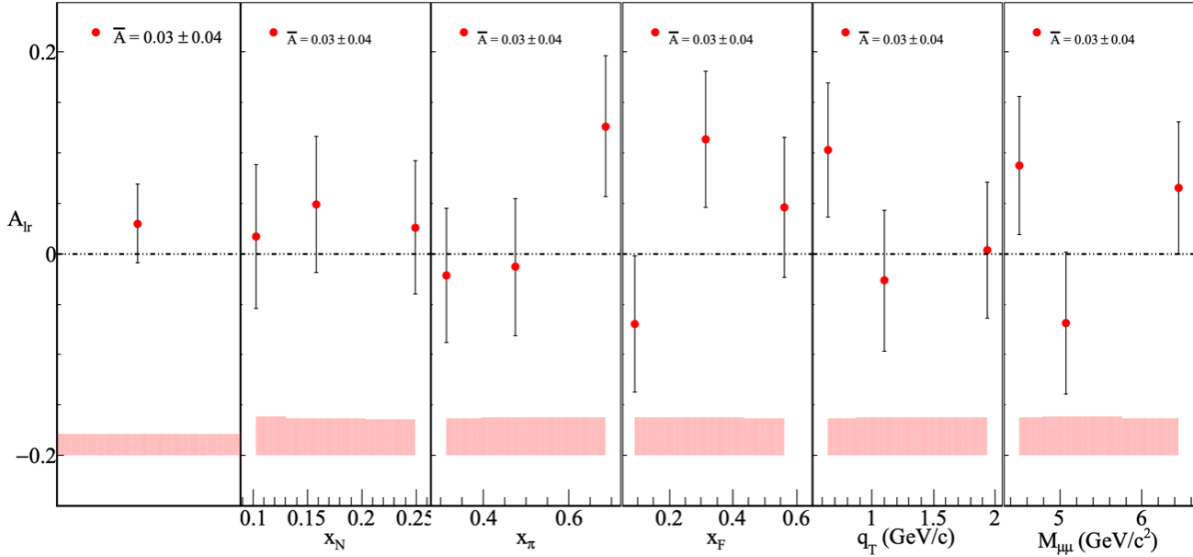


Figure 1.28:  $A_{lr}$  determined by the two-target geometric mean method for all kinematic binnings

statistical error bars are too large to definitively conclude the sign flip is true. There are also no clear trends in the physics kinematic binning due to the large statistical error bars.

It is interesting to note that Eq. 1.41 was derived with the assumption that the leading order Drell-Yan cross-section, Eq. ??, is sufficient. It is not theoretically ruled out however, that the left-right asymmetry

results from higher order amplitudes in addition to the Sivers amplitude. As Fig. 1.29 shows, the left-right asymmetry is slightly less significant about zero than the Sivers amplitude determined from the double ratio method. This could indicate the need to include higher order terms in the Drell-Yan cross-section.

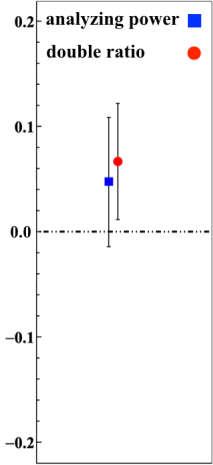


Figure 1.29: The left-right asymmetry adjusted (analyzing power, blue) to be compared with Sivers amplitude determined from the double ratio method (red).

# Appendix A

# Systematic Error Derivations

## A.1 Systematic Error From Acceptance

For an asymmetry defined as

$$A_\alpha = \frac{1}{|S_T|} \frac{\alpha\sigma_l - \sigma_r}{\alpha\sigma_l + \sigma_r} \quad (\text{A.1})$$

where  $\alpha$  is an acceptance ratio.  $\alpha$  is assumed to be close to unity therefore let

$$\alpha = 1 \pm 2\epsilon, \quad (\text{A.2})$$

where  $\epsilon$  is a small positive number. The asymmetry can therefore be written

$$A_\alpha = \frac{1}{|S_T|} \frac{(1 \pm 2\epsilon)\sigma_l - \sigma_r}{(1 \pm 2\epsilon)\sigma_l + \sigma_r} = \frac{1}{P} \frac{\sigma_l - \sigma_r \pm 2\epsilon\sigma_l}{(\sigma_l + \sigma_r)(1 \pm \frac{2\epsilon\sigma_l}{\sigma_l + \sigma_r})}. \quad (\text{A.3})$$

From there Taylor expand the denominator to get

$$\begin{aligned} A_\alpha &\approx \frac{1}{|S_T|} \frac{\sigma_l - \sigma_r \pm 2\epsilon\sigma_l}{(\sigma_l + \sigma_r)} \left(1 \mp \frac{2\epsilon\sigma_l}{\sigma_l + \sigma_r}\right) \\ &= A_{lr} \pm \frac{1}{|S_T|} \frac{2\epsilon\sigma_l}{\sigma_l + \sigma_r} \mp A_{lr} \frac{2\epsilon\sigma_l}{\sigma_l + \sigma_r} \mp \frac{1}{|S_T|} \left(\frac{2\epsilon\sigma_l}{\sigma_l + \sigma_r}\right)^2. \end{aligned} \quad (\text{A.4})$$

Assuming  $A_{lr}$  is small and  $\sigma_l \approx \sigma_r$

$$A_\alpha \approx A_{lr} \pm \frac{\epsilon}{|S_T|}. \quad (\text{A.5})$$

The true asymmetry can now be written

$$A_{lr, systematic} \approx A_\alpha \mp \frac{\epsilon}{|S_T|}. \quad (\text{A.6})$$

Including the  $\frac{\epsilon}{|S_T|}$  term as an additive error and using standard error propagation the systematic error can

be approximated as

$$\delta A_{lr,systematic} = \frac{|\alpha - 1|}{2} \frac{1}{|S_T|} + \frac{\delta_{\frac{|\alpha-1|}{2}}}{|S_T|}. \quad (\text{A.7})$$

## A.2 Systematic Error From Left-Right Event Migration

Assuming the fraction of events miss-identified is  $\gamma$  and that the amount of miss-identified events reconstructed left equals the amount of outgoing events reconstructed right

$$A_{lr,measure} = \frac{1}{|S_T|} \frac{(l + \frac{\gamma}{2} N_{total}) - (r + \frac{\gamma}{2} N_{total})}{(l + \frac{\gamma}{2} N_{total}) + (r + \frac{\gamma}{2} N_{total})} = \frac{1}{|S_T|} \frac{l - r}{(l + r)(1 + \gamma \frac{N_{total}}{l+r})}, \quad (\text{A.8})$$

where  $N_{total}$  is the total events measure,  $l$  is the true events measured to the left that should be measured left and  $r$  is the number of events measure to the right that should be measured to the right.

Assuming  $\gamma$  is a small percentage, the denominator can be Taylor expanded to give

$$A_{lr,measure} \approx A_{lr} \left(1 - \gamma \frac{N_{total}}{l+r}\right). \quad (\text{A.9})$$

Including  $\gamma A_{lr,measure}$  as an additive error and using standard error propagation the systematic error can be approximated as

$$\delta A_{lr,systematic} = \gamma A_{lr,measure} + \gamma \delta A_{lr,measure}. \quad (\text{A.10})$$

# References

- [1] M. Aghasyan et al. First measurement of transverse-spin-dependent azimuthal asymmetries in the Drell-Yan process. *Phys. Rev. Lett.*, 119(11):112002, 2017. doi: 10.1103/PhysRevLett.119.112002.
- [2] M. Anselmino, M. Boglione, U. D'Alesio, F. Murgia, and A. Prokudin. Study of the sign change of the Sivers function from STAR Collaboration W/Z production data. *JHEP*, 04:046, 2017. doi: 10.1007/JHEP04(2017)046.
- [3] Miguel G. Echevarria, Ahmad Idilbi, Zhong-Bo Kang, and Ivan Vitev. QCD Evolution of the Sivers Asymmetry. *Phys. Rev.*, D89:074013, 2014. doi: 10.1103/PhysRevD.89.074013.
- [4] Peng Sun and Feng Yuan. Transverse momentum dependent evolution: Matching semi-inclusive deep inelastic scattering processes to Drell-Yan and W/Z boson production. *Phys. Rev.*, D88(11):114012, 2013. doi: 10.1103/PhysRevD.88.114012.
- [5] Jan Matousek. *Nucleon spin structure studies in Drell-Yan process at COMPASS*. PhD thesis, University of Trieste, April 2018.
- [6] S. Agostinelli et al. Geant4a simulation toolkit. *Nuclear Instruments and Methods in Physics Research Section A: Accelerators, Spectrometers, Detectors and Associated Equipment*, 506(3):250 – 303, 2003. ISSN 0168-9002. doi: [https://doi.org/10.1016/S0168-9002\(03\)01368-8](https://doi.org/10.1016/S0168-9002(03)01368-8). URL <http://www.sciencedirect.com/science/article/pii/S0168900203013688>.
- [7] T. Szameitat. *New Geant4-based Monte Carlo Software for the COMPASS-II Experiment at CERN*. PhD thesis, Albert-Ludwigs-Universitat Freiburg, 2017.